Published in final edited form as:
Neuroscience. 2005 ; 136(1): 65–86.

CONNEXIN-47 AND CONNEXIN-32 IN GAP JUNCTIONS OF OLIGODENDROCYTE SOMATA, MYELIN SHEATHS, PARANODAL LOOPS AND SCHMIDT-LANTERMAN INCISURES: IMPLICATIONS FOR IONIC HOMEOSTASIS AND POTASSIUM SIPHONING

N. KAMASAWA[a], **A. SIK**[b], **M. MORITA**[a], **T. YASUMURA**[a], **K. G. V. DAVIDSON**[a], **J. I. NAGY**[c], and **J. E. RASH**[a,*]

a *Department of Biomedical Sciences, Colorado State University, Fort Collins, CO 80523-1617, USA*

b *Centre de recherche Université Laval Robert-Giffard, 2601 Chemin de la Canardiere, Quebec, Quebec, Canada G1J 2G3*

c *Department of Physiology, Faculty of Medicine, University of Manitoba, 730 William Avenue, Winnepeg, Manitoba, Canada R3E 3J7*

Abstract

The subcellular distributions and co-associations of the gap junction-forming proteins connexin47 and connexin32 were investigated in oligodendrocytes of adult mouse and rat CNS. By confocal immunofluorescence light microscopy, abundant connexin47 was co-localized with astrocytic connexin43 on oligodendrocyte somata, and along myelinated fibers, whereas connexin32 without connexin47 was co-localized with contactin-associated protein (caspr) in paranodes. By thin-section transmission electron microscopy, connexin47 immunolabeling was on the oligodendrocyte side of gap junctions between oligodendrocyte somata and astrocytes. By freeze-fracture replica immunogold labeling, large gap junctions between oligodendrocyte somata and astrocyte processes contained much more connexin47 than connexin32. Along surfaces of internodal myelin, connexin47 was several times as abundant as connexin32, and in the smallest gap junctions, often occurred without connexin32. In contrast, connexin32 was localized without connexin47 in newly-described autologous gap junctions in Schmidt-Lanterman incisures and between paranodal loops bordering nodes of Ranvier. Thus, connexin47 in adult rodent CNS is the most abundant connexin in most heterologous oligodendrocyte-to-astrocyte gap junctions, whereas connexin32 is the predominant if not sole connexin in autologous (“reflexive”) oligodendrocyte gap junctions. These results clarify the locations and connexin compositions of heterologous and autologous oligodendrocyte gap junctions, identify autologous gap junctions at paranodes as potential sites for modulating paranodal electrical properties, and reveal connexin47-containing and connexin32-containing gap junctions as conduits for long-distance intracellular and intercellular movement of ions and associated osmotic water. The autologous gap junctions may regulate paranodal electrical properties during saltatory conduction. Acting in series and in parallel, autologous and heterologous oligodendrocyte gap junctions provide essential pathways for intra- and intercellular ionic homeostasis.

Keywords

confocal microscopy; freeze fracture; immunofluorescence; immunogold labeling; rodent

*Corresponding author. Tel: +1-970-491-5606; fax: +1-970-491-7907. E-mail address: john.rash@colostate.edu (J. E. Rash)..

Abbreviations

A/A, astrocyte-to-astrocyte; AQP4, aquaporin4; caspr, contactin-associated protein; Cx, connexin, designated according to molecular weight in kiloDaltons; Cx26, connexin26; Cx29, connexin29; Cx30, connexin30; Cx32, connexin32; Cx43, connexin43; Cx47, connexin47; DAB, diaminobenzidine; E-face, extraplasmic leaflet; FRIL, freeze-fracture replica immunogold labeling; GFAP, glial acidic fibrillary acidic protein; IMP, intramembrane particle/intramembrane protein; KO, knockout; LE, labeling efficiency; LM, light microscopy; O/A, oligodendrocyte-to-astrocyte; O/O, oligodendrocyte-to-oligodendrocyte; PB, phosphate buffer; P-face, protoplasmic leaflet; PNS, peripheral nervous system; TBST, Tris-HCl-buffered saline with Triton X-100; TEM, transmission electron microscopy

Gap junctions are clusters of intercellular channels that allow direct cell-to-cell passage of ions and small molecules (Goodenough et al., 1996). In rodents and humans, gap junctions are formed by 20 or 21 different connexin (Cx) proteins (Willecke et al., 2002), often consisting of two or three different connexins in each gap junction hemi-plaque (Severs, 1999; Nagy et al., 2004; Rash et al., 2004b). Intercellular channels formed by different connexins have distinct conductances, permeabilities to different molecules, and different modes of regulation (Veenstra, 1996; White and Bruzzone, 1996; Coppen et al., 2003). Since not all connexins form permissive channels with each other (White and Bruzzone, 1996), differential distribution of multiple connexins may confer selectivity for gap junctional intercellular communication pathways between different cell types in heterogeneous tissues (White and Bruzzone, 2000; Söhl and Willecke, 2003), particularly in the CNS, where multiple connexins within gap junctions link macroglial cells into a “functional syncytium” (Mugnaini, 1986; Rash et al., 2001). Homologous astrocyte-to-astrocyte (A/A) gap junctions abundantly express connexin30 (Cx30) and connexin43 (Cx43) (Yamamoto et al., 1990a,b; Bruzzone and Goodenough, 1995; Ochalski et al., 1997; Kunzelmann et al., 1999; Nagy and Rash, 2000; Rash et al., 2001) and modest amounts of connexin26 (Cx26) (Nagy et al., 2001; Altevogt and Paul, 2004); but see (Mercier and Hatton, 2001; Condorelli et al., 2003; Filippov et al., 2003). Although homologous oligodendrocyte-to-oligodendrocyte (O/O) gap junctions are rare or nonexistent (Mugnaini, 1986; Rash et al., 1997, 2001), oligodendrocytes are extensively coupled to astrocytes at heterologous oligodendrocyte-to-astrocyte (O/A) gap junctions, where the oligodendrocyte plaques contain connexin32 (Cx32) and connexin47 (Cx47) (Scherer et al., 1995; Li et al., 1997; Rash et al., 1997, 2001; Nagy and Rash, 2000, 2003; Menichella et al., 2003; Odermatt et al., 2003; Nagy et al., 2004) and possibly connexin29 (Cx29) (Nagy et al., 2003a,b; Altevogt and Paul, 2004; Kleopas et al., 2004). Although Cx29 is found in hexagonal “rosettes” of intramembrane particles (IMPs) in the innermost layer of myelin (Li et al., 2002), it has not been demonstrated in ultrastructurally-defined gap junctions. Functional importance of glial connexins is indicated by gross structural abnormalities in myelin sheaths of Cx32/Cx47 double-knockout (KO) mice and Cx47 KO mice, and physiological deficits in Cx30, Cx32 and Cx43 KO mice (Scherer et al., 1998; Bahr et al., 1999; Menichella et al., 2003; Odermatt et al., 2003; Dere et al., 2003; Theis et al., 2003).

To understand the bases for the neurological deficits created by deletion or alteration of oligodendrocyte connexins, it is essential to determine the ultrastructural organization and connexin composition of gap junctions at different loci within the panglial syncytium. Unresolved are the relative abundances of Cx47 and Cx32 at all O/A junctions, as well as the relative contributions of these connexins to O/A coupling. In addition, the existence and composition of intracellular (or autologous) gap junctions between cytoplasmic myelin layers at paranodes and Schmidt-Lanterman incisures in normal tissues remain uncertain. In this study, we used confocal light microscopy (LM), thin-section transmission electron microscopy (TEM) and freeze-fracture replica immunogold labeling (FRIL) to localize Cx47 and Cx32 in

normal rat and mouse CNS. We demonstrate much greater abundance of Cx47 than Cx32 in heterologous O/A gap junctions, provide the first ultra-structural demonstrations of autologous gap junctions between myelin layers in Schmidt-Lanterman incisures and between successive paranodal loops, and show that autologous gap junctions contain primarily or exclusively Cx32. These data also provide a plausible basis for understanding the pathological swelling of myelin, convulsions, and death that occur in Cx32/Cx47 double-KO mice, all apparently resulting from complete loss of essential gap junction pathways for redistributing the excess potassium ions and associated osmotic water that enter myelin during normal axonal electrical activity.

EXPERIMENTAL PROCEDURES

Antibodies and animals

The antibodies used in this study, together with sources and references, are listed in Table 1. A total of 35 adult male CD1 mice and 14 male Sprague–Dawley rats (120–250 g) were used for immunofluorescence and thin-section electron microscopic immunocytochemistry studies, and one female and three male rats were used for FRIL studies, according to protocols approved by the Central Animal Care Committees at our respective institutions. All animal experiments were carried out in accordance with the National Institute of Health Guide for the Care and Use of Laboratory Animals (NIH Publications No. 80-23) revised 1996. All efforts were made to minimize the number of animals used and to minimize their pain or suffering.

LM immunohistochemistry

Mice and rats were deeply anesthetized with Equithesin (3 ml/kg) and perfused transcardially with 3 ml of “prefixative” solution consisting of cold (4 °C) 25 mM sodium phosphate buffer, pH 7.4, 0.9% NaCl (PBS), 0.1% sodium nitrite and heparin (1 unit/ml). This was followed by perfusion with 20 or 40 ml of cold 160 mM sodium phosphate buffer, pH 7.4, containing 2% freshly depolymerized paraformaldehyde (i.e. formaldehyde) and 0.2% picric acid, followed by perfusion with 10 ml of 25 mM phosphate buffer (PB), pH 7.4, containing 10% sucrose. Brains were removed and stored at 4 °C for 48 h in cryoprotectant (10% sucrose in 25 mM PB). Cryostat sections (10 μm thick) were collected on gelatinized glass slides, and processed for immunofluorescence microscopy using primary and secondary antibodies diluted in 50 mM Tris–HCl, pH 7.4, containing 1.5% NaCl, 0.3% Triton X-100 (TBST) and 4% normal donkey serum.

For double immunofluorescence labeling of Cx47 in combination with either Cx32 or Cx43, sections were incubated for 24 h at 4 °C with a newly-available monoclonal anti-Cx47 (37-4500) and simultaneously with either polyclonal anti-Cx32 71-600 (2 μg/ml), polyclonal anti-Cx32 34-5700 (2 μg/ml), polyclonal anti-Cx43 71-0700 (2 μg/ml) (all from Zymed Laboratories Inc., South San Francisco, CA, USA; now Invitrogen/Zymed) or polyclonal anti-Cx43 18A (diluted 1:3000) (Yamamoto et al., 1990a,b). Alternatively, and with similar results obtained (not shown), sections were incubated for 24 h at 4 °C with polyclonal anti-Cx47 36-4700 (2 μg/ml) and simultaneously with either monoclonal anti-Cx32 35-8900 (2 μg/ml) or monoclonal anti-Cx43 35-5000 (2 μg/ml) (all from Zymed). The availability of both monoclonal and polyclonal antibodies to Cx47 permits a greater variety of double- and triple-labeling experiments to be conducted. For double immunofluorescence labeling of caspr in combination with Cx32 or Cx47, sections were incubated for 24 h at 4 °C with monoclonal anti-caspr (Peles et al., 2005) and simultaneously with either polyclonal anti-Cx32 34-5700 (2 μg/ml) or polyclonal anti-Cx47 36-4700 (2 μg/ml). Sections were washed in TBST for 1 h at room temperature and incubated simultaneously with FITC-conjugated donkey anti-mouse IgG diluted 1:200 (Jackson ImmunoResearch Laboratories, West Grove, PA, USA) and Cy3-conjugated donkey anti-rabbit IgG (Jackson) diluted 1:200. For triple immunofluorescence labeling, sections were incubated simultaneously with goat anti-Cx43 (Santa Cruz Biotech,

Santa Cruz, CA, USA) at a dilution of 2 μg/ml, and with mouse monoclonal anti-caspr and rabbit anti-Cx47 as above. Sections were washed and then incubated simultaneously with Cy3-conjugated donkey anti-goat IgG (Jackson) diluted 1:200, FITC-conjugated donkey anti-mouse IgG diluted 1:200, and Cy5-conjugated donkey anti-rabbit IgG (Jackson) diluted 1:200. Sections were washed for 20 min in TBST, followed by two 20 min washes in 50 mM Tris–HCl buffer, pH 7.4, and coverslipped with antifade medium. To establish absence of inappropriate cross-reactions of primary with secondary antibodies, control procedures included omission of one of the primary antibodies with inclusion of each of the secondary antibodies.

Fluorescence was examined on a Zeiss Axioskop2 fluorescence microscope with image capture using Axiovision 3.0 software (Carl Zeiss Canada, Toronto, Canada), and an Olympus Fluoview IX70 confocal microscope with image capture using Olympus Fluoview software. For confocal analysis, double-labeled sections were scanned twice using single laser excitation for each fluorochrome scan. Images were assembled using either Photoshop 6.0 or Corel Draw 8, and pseudocoloring was with Northern Eclipse software (Empix Imaging, Mississauga, ON, Canada).

Thin-section immunoperoxidase and immunogold labeling

Mice were deeply anesthetized with ketamine/xylazine cocktail and perfused through the aortic arch with 0.9% NaCl followed by a fixative solution containing 4% formaldehyde (Sigma-Aldrich, Germany), 0.05% glutaraldehyde (TAAB Laboratories, Aldermaston, UK) and 0.2% picric acid (Sigma-Aldrich, Oakville, Canada) in 0.1 M PB (pH 7.4). Brains were removed, coronal blocks were dissected from the midbrain, and sections 60 μm thick were cut from the blocks with a vibrating microtome (Leica, Wetzlar, Germany). Sections were washed in 0.1 M PB and immersed in 30% sucrose overnight, freeze-thawed over liquid nitrogen (to optimize penetration of immunoreagents), rinsed in PB and Tris-buffered saline (0.05 M, pH 7.4), and incubated with rabbit anti-Cx47 (Table 1). After 48–72 h incubation, sections were washed and incubated for 12 h at 4 °C either with 1 nm gold-conjugated anti-rabbit secondary antibody (diluted 1:200; Aurion, Wageningen, Netherlands) followed by silver intensification (SE-EM, Aurion), or for 2 h with biotinylated anti-rabbit or anti-mouse IgG (diluted 1:500;Vector Laboratories, Burlingame, CA, USA) followed by reaction for 1.5 h with avidin-biotinylated horseradish peroxidase complex (diluted 1:1000; Elite ABC, Vector Laboratories). The immunoperoxidase reaction was developed using 3, 3′ diaminobenzidine (DAB) (Sigma-Aldrich) and intensified with ammonium nickel-sulfate (DAB-Ni) as a chromogen.

Sections were treated with 1% osmium-tetroxide in 0.1 M PB for 1 h, dehydrated in ethanol and propylene-oxide, and embedded in Durcupan (ACM, Fluka AG, Buchs, Switzerland). During dehydration, the sections were stained with 1% uranyl acetate (Sigma-Aldrich, Germany) in 70% ethanol for 45 min. Selected immunoreactive profiles were re-embedded for ultrathin sectioning using a Leica Ultracut S. Electron micrographs were obtained using a Philips Tecnai 12 microscope equipped with MegaView II digital camera.

FRIL

For FRIL, one adult female and three adult male Sprague–Dawley rats were anesthetized with ketamine/xylazine (90 mg/kg and 8 mg/kg) and fixed by transcardiac perfusion with 2% or 4% formaldehyde in Sorenson's PB (pH 7.4). For technical reasons, glutaraldehyde fixation cannot be used for FRIL (Rash and Yasumura, 1999). Samples of spinal cord were sliced at 150 μm-thick using a Lancer 3000 refrigerated Vibratome (Technical Products International, St. Louis, MO, USA), cryoprotected with 30% glycerol, frozen by contact with a liquid nitrogen-cooled metal mirror, and freeze-fractured and replicated in a JEOL/RMC RFD 9010C freeze-fracture device. After replication and before samples were thawed, a gold "index" grid containing a

suspended droplet of 3% Lexan dissolved in ethylene dichloride was placed on the replicated tissue, and the solvent was evaporated overnight as the sample temperature was raised to −35 °C (Rash et al., 1995). Samples (with grid firmly attached in Lexan plastic) were thawed, mapped using a Zeiss LSM510 confocal microscope, cleaned at 50 °C by vigorous stirring for 29 h in 2.5% sodium dodecylsulfate detergent, rinsed in blocking buffer, and immunogold labeled (Rash and Yasumura, 1999; Rash et al., 2001; Pereda et al., 2003). Replicas were single labeled with rabbit polyclonal antibodies against Cx47 (Zymed) or double-labeled with mouse monoclonal antibodies against Cx32 (Chemicon International, Temecula, CA, USA) and Cx47 (Zymed) or with mono-clonal anti-Cx32 (Chemicon) plus polyclonal anti-Cx29 (Zymed). Secondary immunogold-labeling was with various combinations of goat anti-mouse and goat anti-rabbit IgG bound to 6 nm, 12 nm and/or 18 nm gold (Jackson).

Electron microscopy of FRIL samples

Labeled replicas were rinsed, air dried, coated on the labeled side with 10–20 nm of carbon (to stabilize gold labels and to anneal thermal expansion cracks formed in the replica when warmed from −170 °C to room temperature); the Lexan support film was removed by washing for 2–3 h in dichloroethane; and the samples were air dried and examined at 100 kV in JEOL 2000 EX-II or JEOL 1200 EX TEMs equipped with 60° and 45° tilting stages, respectively. Images were photographed as stereoscopic pairs (8° included angle). High-resolution digital images (20–80 Mbyte) were captured directly from electron microscope negatives using an ArtixScan 2500f digital scanning device (Microtek, Carson, CA, USA). Images were prepared with Photoshop 7.01 (Adobe Systems, San Jose, CA, USA), using minimal “unsharp mask,” maximal contrast expansion with “levels” and by selected area “dodging” using “brightness/contrast” functions to optimize image contrast and definition. Selected images are presented as stereoscopic pairs to allow discrimination of 6 nm gold beads from equally-electron-opaque, platinum-shadowed 6–10 nm IMPs. To better reveal connexon extraplasmic leaflet (E-face) pits (which do not cast shadows, and hence are much more difficult to discern than their corresponding protoplasmic leaflet (P-face) IMPs, which do cast shadows), one group of gap junction images is presented both with white shadows, as well as with black shadows, according to the original convention of (Steere 1957). In black-shadow images, pits are black and particles cast black shadows (as in nature), but immunogold beads appear anomalously white.

Detectability vs. labeling efficiency (LE) of different sizes of immunogold beads

In most experiments, the use of two or more size classes of immunogold beads to label each connexin facilitated detection of gap junctions in low magnification searches based on higher visibility of the larger gold beads, yet retained the higher LE of the smaller gold beads (Nagy et al., 2001). LE for gap junctions, as defined in Rash and Yasumura (1999), is the ratio of the number of immunogold beads to the number of connexons. Typically, LE for 10 nm or 12 nm gold beads varies from 1:4–1:30 in Cx43-containing A/A gap junctions (Rash et al., 2001), but is much lower in gap junctions that have connexins expressed at low levels (such as Cx26 or Cx30) and in junctions labeled with 18 nm or 30 nm immunogold beads (Nagy et al., 2001). In the current FRIL replicas, “signal-to-noise” ratios (defined in Rash and Yasumura, 1999) were 500:1–5000:1. Under similar conditions used for semi-quantitative analysis, 6 nm, 12 nm and 18 nm immunogold beads labeled at a ratio of ca. 4:2:1 (Nagy et al., 2004). However, 6 nm gold beads are not detectable at 10,000× on the TEM viewscreen when viewed with 10-power binoculars, and 12 nm gold beads are faintly detectable, whereas 18 nm gold beads are readily detected based on their large diameter and disproportionately greater electron opacity. Because both cross-sectional area and electron opacity increase with the square of the diameter, “detectability” of labels increases with the fourth power of the diameter. Consequently, 18 nm gold beads were used primarily to detect (i.e. find) labeled gap junctions, whereas the higher efficiency labeling of 6 nm and 12 nm gold beads was used for semi-quantitative analysis of LE. However, stochastic processes limit the use of larger gold beads for semi-quantitative

analysis, except in the largest gap junctions, which were labeled by multiple large gold beads. Thus, we often combined 6 nm and 18 nm gold beads for labeling one connexon and used 12 nm beads for the second label. This procedure provided a second advantage in that the simultaneous presence of two sizes of gold beads for the primary connexin of interest provided an internal verification of labeling specificity for that connexin and its primary antibody. Nevertheless, it is likely that because of the visibility threshold for small gold beads, a few small gap junctions (<20 connexons) that were labeled by only a few 6 nm gold beads were not detected because they were not accompanied by one or more 12 nm or 18 nm gold beads. (For examples, see sections on gap junctions in paranodes and Schmidt-Lanterman incisures).

RESULTS

Immunofluorescence localization of Cx32 and Cx47 on oligodendrocyte somata and myelin

We previously reported a differential distribution of punctate immunofluorescence labeling for Cx47 in white and gray matter of *mouse* brain. Oligodendrocyte somata were heavily laden with Cx47 in both white and gray matter, whereas white matter and myelinated fibers passing through gray matter contained far less Cx47 compared with the high concentrations of Cx29 and Cx32 associated with these structures (Li et al., 2004). To further assess potential differences in regional connexin expression, we examined Cx32 and Cx47 immunofluorescence in gray and white matter of *rat* brain and spinal cord. Oligodendrocyte somata throughout gray matter of spinal cord displayed intense punctate labeling for both Cx32 and Cx47 around their peripheries, with Cx47 puncta somewhat larger than Cx32 puncta (Fig. 1A). Oligodendrocyte somata in white matter were intensely decorated with Cx47-immunopositive puncta, similar to those in gray matter (Fig. 1B1), whereas Cx32-positive puncta on these cells were generally smaller, fewer and less intensely labeled (Fig. 1B2). The two connexins were often co-localized on somata in both gray and white matter, except where Cx47 appeared in the absence of Cx32 in some areas of white matter, and to a lesser degree, where a few puncta were labeled for Cx32 but not Cx47 (Fig. 1A3 and 1B3).

Myelinated fibers traversing through gray matter in rat CNS showed a similar paucity of Cx47 as that seen previously in mouse brain. However, white matter areas such as the corpus callosum (Fig. 1C), in addition to containing dense labeling for Cx47 associated with oligodendrocyte somata, also contained higher densities of dispersed, fine Cx47 puncta (Fig. 1C1) than seen in these same areas of mouse brain, and contained typically dense concentrations of Cx43 puncta (Fig. 1C2). Laser scanning confocal double-immunofluorescence labeling for Cx47 and Cx43, conducted to determine whether fine Cx47-positive puncta were associated with astrocytic Cx43 in white matter, revealed substantial co-localization of these two connexins (Fig. 1D). Similarly dispersed punctate labeling for Cx47 was observed in rat spinal cord white matter, and double labeling revealed substantial co-localization of these puncta with astrocytic Cx43 (Fig. 1E).

Localization of Cx47 by thin-section TEM

The cellular localization and intracellular distribution of Cx47 was examined using pre-embedding immunoperoxidase methods. Samples for analysis were taken from various cerebral cortical regions and from the thalamus, all yielding similar results. Immunolabeling was associated exclusively with oligodendrocytes, and nearly all DAB immunoreaction product was found in restricted deposits in close proximity to plasma membranes of these cells (Fig. 2A). At such deposits, gap junctions were frequently identified between the oligodendrocyte membrane and processes identified as astrocytic based on their small size, electron lucent cytoplasm, flattened cross-section and absence of synaptic vesicles (Fig. 2B, C). The distance between the membranes of oligodendrocytes and astrocytes at gap junctions was 2.62 nm (standard deviation, 0.42 nm; *n*, 15). Immunoperoxidase reaction product for

Cx47 was always localized on the oligodendrocyte side of gap junctions and never on the astrocyte side. Occasionally, Cx47-reaction product was also seen dispersed around endoplasmic reticulum (Fig. 2A). Cx47 immunolabeling was not detected by thin-section EM in myelin sheaths in any mouse brain structures examined (but see rat FRIL data, below).

Pre-embedding immunogold analysis of the subcellular locations of Cx47 revealed silver-intensified gold particles distributed along the inner side of the plasma membrane of oligodendrocytes (Fig. 2D), where gap junctions were shared with presumptive astrocyte processes (Fig. 2E, F). Immunolabeling was not observed between adjacent oligodendrocytes, or on the astrocyte side of O/A gap junctions. Silver-intensified gold particles were rarely observed in membrane-delineated structures in oligodendrocyte cytoplasm or in myelin sheaths, where labeling associated with both of these structures was close or equivalent to the level of background signal.

FRIL revealed Cx32 and Cx47 in gap junctions on oligodendrocyte somata

Two replicas of adult rat spinal cord that were double-labeled for Cx32+Cx47 using alternately reversed sizes of gold were searched quantitatively by FRIL, and several additional samples single-labeled for Cx47 were examined qualitatively. Oligodendrocyte somata (Fig. 3A) were identified based on their intermediate cell diameter (10–15 μm), which when cross-fractured, usually revealed a relatively thin layer of cytoplasm devoid of bundles of intermediate filaments (i.e. glial acidic fibrillary acidic protein (GFAP) filaments in astrocytes) or extensive stacks of rough endoplasmic reticulum (i.e. Nissl substance in neurons). Criteria for identifying cell types in freeze-fracture replicas are documented in Rash et al. (1995). The cell soma was identified by the presence of the cell nucleus, either in cross-section (not shown) or in fractures within the inner or outer nuclear membranes (Fig. 3A). Gap junctions linking oligodendrocyte somata to astrocyte processes contained from a few connexons (not shown) to more than 2000 connexons (Fig. 3B), the latter displaying robust immunogold labeling for Cx47. Because of the shadow cast by a displaced tissue fragment (immediately outside the area shown), a large portion of the gap junction in this image was not shadowed by platinum, but nevertheless, was faintly delineated by the secondary carbon coat, as previously shown (Rash and Yasumura, 1999) (Fig. 3A; three arrowheads define the margin of the gap junction). Immunogold labeling of Cx47 in large gap junctions was 10-fold to as much as 100-fold higher than that of Cx32. For example, in this one somatic gap junction, Cx47 was labeled by 136 12 nm gold beads, whereas Cx32 was labeled by zero 6 nm gold beads and only one 18 nm gold bead (Fig. 3B). (In this area, which was coated with carbon but not shadowed with platinum, 6 nm gold beads, if present, would have been easily discerned above the low electron opacity of carbon.) In the same sample, labeling for Cx32 was robust in other classes of oligodendrocyte gap junctions, such as autologous gap junctions (see below), suggesting that low levels of Cx32 labeling (vs. Cx47 labeling) in some somatic O/A gap junctions was not an artifact of vastly different labeling efficiencies of the primary antibodies or of the different sizes of immunogold labels.

Cx47 in “oligodendrite” gap junctions

A few cytoplasmic branches (“dendrites”) extend from oligodendrocyte somata to one or more segments of internodal myelin. In FRIL replicas, these “oligodendrites” were identified by their elongate, relatively constant small diameter (usually<2 μm; Fig. 4A), direct continuity with the outer layer of one or more myelin sheaths (Fig. 4A, arrow), and abundant gap junctions (Fig. 4A–D). Large gap junctions labeled for Cx47 by a high density of immunogold beads were particularly prominent. Seven immunogold-labeled gap junctions on a portion of one oligodendrite (Fig. 4A) contained from <30 (Fig. 4C) to ca. 200 connexons (Fig. 4B), with other dendrites having gap junctions containing >1000 connexons (Fig. 4D).

Cx32 and Cx47 in gap junctions on myelin outer surfaces

In FRIL samples of adult rat spinal cord that had been double-labeled for Cx47 and Cx32, the external plasma membranes of myelin were identified by their extensive particle-free areas (Fig. 5A–F), by multiple "reciprocal patches" of mixed IMPs and pits in both E- and P-faces (Fig. 5A), and by tight junctions linking the outer tongue to the second wrapping of myelin (not shown, but see Sandri et al., 1977; Schnapp and Mugnaini, 1978; Rash et al., 1997). In all cases where a cell process coupled to the outer surface of myelin could be identified, each was found to be astrocytic based on the presence of bundles of distinctive cytoplasmic intermediate GFAP filaments and/or aquaporin4 (AQP4) square arrays (Rash et al., 1998, 2004a) in its plasma membrane (Fig. 5B, C). Immunogold labeling for Cx47 revealed that gap junctions were abundant on myelin, where by FRIL, they were more abundant than at all other locations (Table 2). However, most gap junctions on myelin were small, usually <100 connexons (Fig. 5D), but occasionally contained from 200 (Fig. 5B, C) to >1000 connexons (Rash et al., 2001). Of those on myelin, 66% were labeled exclusively for Cx47 (Fig. 5A–C), 21% were double-labeled for Cx47+Cx32 (Fig. 5D), and only 13% were labeled exclusively for Cx32 (Fig. 5E–F; data summarized in Table 2).

Immunofluorescence imaging of caspr and Cx32 along myelinated fibers

The protein caspr is selectively concentrated in paranodal regions at nodes of Ranvier (Einheber et al., 1997; Peles et al., 2005). Possible co-association of caspr with Cx32 and/or Cx47 was examined in sagittal sections of rat spinal cord by double immunofluorescence labeling. Low magnification confocal micrographs of white matter revealed robust labeling for caspr along myelinated fibers at presumptive nodes of Ranvier (Fig. 6A1). Labeling for Cx32 was much more widely distributed along these fibers, and had a fine granular appearance (Fig. 6A, B). Dense labeling for caspr at paranodes occasionally overlapped with labeling for Cx32 (Fig. 6A, B). From a survey of various regions of spinal cord white matter, it was evident that Cx32 was co-localized at caspr-positive paranodes in ventrolateral (Fig. 6C) and ventral column white matter areas (Fig. 6D), and in the dorsal columns (Fig. 6E), thereby providing additional evidence that the paired areas stained for Cx32 correspond to paranodal caspr-immunopositive areas. In addition, internodal regions not labeled for caspr often had funnel-shaped bands of Cx32 immunofluorescence extending from the surface of myelin to near the central axon (Fig. 6B2). Some of these Cx32-positive puncta may correspond to Cx32-containing gap junctions at Schmidt-Lanterman incisures (see next paragraph).

Cx32 in gap junctions at Schmidt-Lanterman incisures

Schmidt-Lanterman incisures are small cytoplasmic expansions that spiral from the outer tongue of myelin to the inner tongue, forming a continuous conduit of cytoplasm from the outermost to innermost layers of myelin (Sandri et al., 1977; Mugnaini et al., 1977; Massa and Mugnaini, 1982). High-magnification FRIL searches revealed several very small autologous (or "reflexive") gap junctions between the 2nd and 3rd innermost layers of myelin at an incisure (Fig. 7A–E). Consisting of seven to 24 E-face pits each, these gap junctions were labeled for Cx32 by a total of seven 6 nm gold beads and one 18 nm gold bead. In contrast, Cx47 (12 nm gold) was not detected at these locations, despite its greater abundance in most other heterologous O/A gap junctions elsewhere in the same sample (Fig. 3 and Fig. 5). This immunogold labeling for Cx32 at reflexive gap junctions at Schmidt-Lanterman incisures contrasts with the virtual absence of 6 nm gold beads (for Cx32) in some of the much larger O/A gap junctions, where 12 nm gold beads for Cx47 were abundant (Fig. 3B, 5A–C). It is also noteworthy that autologous gap junctions in Schmidt-Lanterman incisures had a much higher "LE" for Cx32 (LE, 1:5 or eight gold beads labeling ca. 42 connexons) than most heterologous junctions (LE, 1:30–1:100). The extraordinarily high LE for Cx32 and absence

of labeling for Cx47 at gap junctions in Schmidt-Lanterman incisures suggests that these junctions are composed primarily, if not exclusively, of Cx32.

Cx32 demonstrated in gap junctions linking successive paranodal loops

In ascending and descending white matter tracts of spinal cord, myelinated axons were often cross-fractured (Fig. 8A), occasionally exposing nodes of Ranvier (not shown) and internal views of widened paranodal loops (Fig. 8A–D). At identified paranodes, the outer layers of cross-fractured compact myelin (Fig. 8A; M) surrounded the concave expanded loops of paranodal membranes (Fig. 8A). The number of layers of compact myelin outside the paranodal loops indicates that these two widened layers of concave toroidal membrane represent the approximate 24th through 26th paired membrane wrappings of myelin. Moreover, absence of layers of cross-fractured myelin between the axolemma and the concave paranodal loops confirms that this image was not from a Schmidt-Lanterman incisure, which would have had multiple layers of compact myelin both inside and outside the widened and recurvate membranes of the incisure. Unusual linear or “string” gap junctions between successive paranodal loops of myelin (Fig. 8A–C, E) were detected solely because of the presence of immunogold beads for Cx32. Despite double-labeling of this sample for Cx32+Cx29, these paranodal gap junctions were immunogold labeled for Cx32, only. Moreover, in several samples single-labeled for Cx47, no examples of Cx47 labeling of autologous paranodal gap junctions were found, and in double-labeled samples where overall Cx47 labeling was five-fold greater than for Cx32, no Cx47-labeled autologous gap junctions were found. (See below for numerical data regarding labeling efficiencies for small gap junctions.)

Paranodal string gap junctions were oriented circumferentially (i.e. in a direction parallel to myelin wrapping; Fig. 8B–C), as well as radially (i.e. in a direction perpendicular to myelin wrapping; Fig. 8E). “String” gap junctions were first identified and defined in retinal neurons (Raviola and Gilula, 1973; Nagy et al., 2004; Rash et al., 2004b). In oligodendrocytes, these linear arrays of IMPs were identified as string gap junctions, rather than as tight junctions (Fig. 8D), based on the following: i) As in other rodent gap junctions fixed by formaldehyde, 100% of the constituent IMPs were in the P-face (Fig. 8C), and the E-face views consisted entirely of pits (Fig. 8B); ii) the constituent P-face IMPs were 8 –9 nm in diameter and had a uniform 10 nm center-to-center spacing (Fig. 8C), and the E-face pits were uniformly 7–9 nm in diameter and had a uniform 10 nm center-to-center spacing (Fig. 8B); iii) where the fracture plane stepped from E-face to P-face (Fig. 8E), the string of E-face pits was aligned and apparently continuous with the string of P-face IMPs; and iv) the rows of P-face IMPs and E-face pits were labeled for Cx32, consistent with labeling for Cx32 in other oligodendrocyte gap junctions. By way of comparison, both P- and E-face images of *tight junctions* in formaldehyde-fixed samples consist of discontinuous rows of partially-fused IMPs (Fig. 8D), intermixed with short segments of narrow grooves (Fig. 8D). Because of limited protein cross-linking in formaldehyde-fixed tissues, the resulting “particle partitioning coefficient” (Satir and Satir, 1979) for tight junction proteins (claudins and occludins) is reduced to ca. 0.5, causing about half of the particles to fracture to the E-face and half to fracture to the P-face (Saitou et al., 1997; Itoh et al., 1999; Meier et al., 2004), whereas the unchanged particle partitioning coefficient of 1.0 for connexons continues to result in 100% of connexon IMPs remaining with the P-faces.

Immunofluorescence imaging of Cx47 on shoulders of paranodes

Low-magnification double-immunofluorescence imaging of caspr/Cx47 in lateral white matter of rat spinal cord revealed discrete labeling for caspr at paranodes along myelinated fibers (Fig. 9A1) and dispersed punctate labeling for Cx47 (Fig. 9A2), which was in contrast to the often continuous and granular labeling of Cx32 detected along myelinated fibers. Although overlap of caspr-positive areas with some Cx47-positive labeling was evident at low magnification

(Fig. 9A3), higher magnification revealed that Cx47-positive puncta usually were closely apposed to but not entirely overlapping with labeling for caspr, particularly along large diameter fibers in lateral (Fig. 9B) and ventral (Fig. 9C) white matter, as well as along smaller diameter fibers in lateral white matter (Fig. 9D). Since caspr is associated with axonal membranes at paranodes (Einheber et al., 1997;Peles et al., 2005), labeling for this protein occurs central to the paranodal loops. In contrast, Cx47-positive puncta often were at the lateral edges of paranodes (Fig. 9B–D), apparently reflecting the two-dimensional projection of O/A gap junction puncta located at more lateral radial locations—i.e. on the shoulders of the outermost paranodal membrane loops (Waxman and Black, 1984), or in everted paranodal loops (see FRIL, below).

Immunofluorescence co-localization of Cx47 with Cx43

Localization of Cx43 in relation to caspr and Cx47 was examined by triple immunofluorescence labeling (Fig. 9E). At caspr-positive fiber segments (Fig. 9E1), Cx43-positive puncta were occasionally seen straddling the paranodal and juxaparanodal regions (Fig. 9E2), with overlap of these puncta and Cx47-positive puncta (Fig. 9E3 and 9E4). In addition, numerous examples were encountered where labeling for Cx43 occurred within the nodal area, sandwiched between caspr-positive juxtaparanodal segments (Fig. 9E2 and 9E4), presumably reflecting presence of Cx43 at gap junctions between astrocyte processes known to be closely associated with, and concentrated at, the nodal membrane at nodes of Ranvier (Waxman and Black, 1984). White areas (Fig. 9E4) represent areas of triple co-association of Cx47 (blue) and Cx43 (red) at O/A gap junctions superimposed on caspr-positive (green) paranodes.

FRIL detection of Cx47 in heterologous gap junctions on everted paranodal loops

Although paranodal loops are most often completely enclosed within paranodes, the last few paranodal loops are frequently everted (Mugnaini et al., 1977; Schnapp and Mugnaini, 1978; see also Sandri et al., 1977), and gap junctions in these locations are thought to couple with nearby astrocyte processes in both normal paranodes (Waxman and Black, 1984; Black and Waxman, 1988) and in paranodes altered by deletion of caspr (Rios et al., 2003). In FRIL images, gap junctions on everted paranodal loops were labeled for Cx47 (Fig. 10) and, in a separate study, were also labeled for Cx32 (J. E. Rash and S. Royer, unpublished observations). The presence of heterologous O/A gap junctions on everted paranodal loops suggests that the everted loops do not represent a fixation artifact, but either: a) a relatively less common but stable configuration wherein the outermost layer of myelin was unable to completely envelop a preexisting paranodal loop because it was structurally coupled via a gap junction to an adjacent astrocyte process, or b) a transient state wherein osmotically-swollen paranodal loops evert, contact and couple with the astrocyte syncytium as a way of divesting themselves of excess ions and water. Although such instantaneous coupling would require the pre-existence of substantial unassembled Cx47 in paranodal membranes, we have been unable to detect Cx47 in internal (non-everted) paranodal membranes, making this possibility less likely.

Cx32 and Cx47 in six subcellular regions of oligodendrocytes

Quantitative analyses of immunogold-labeled gap junctions, including connexin compositions, numbers of gold beads for each connexin and numbers of connexons in each class of gap junction are presented in Table 2 and Fig. 11, and the subcellular locations of oligodendrocyte gap junctions are shown diagrammatically in Fig. 12. The histogram (Fig. 11, left panel) was derived from two samples that were double-labeled for Cx32+Cx47, with sizes of gold beads reversed for the two experiments, thereby at least partially compensating for the effects of the different labeling efficiencies for different sizes of gold beads (see Experimental Procedures). In these paired samples, a total of 72 gap junctions were found: 13 heterologous gap junctions

(18%) were on oligodendrocyte somata and dendrites (as in Figs. 3 and 4) and 56 (78%) were on the outer surface of myelin (as in Fig. 5). Of these 69 heterologous gap junctions, 26% were double-labeled for Cx47 and Cx32, whereas 59% were labeled exclusively for Cx47, and 15% were labeled exclusively for Cx32. Moreover, the labeling ratio for Cx47: Cx32 in gap junctions on somata and dendrites was 2.7:1, whereas for gap junctions on myelin, the ratio was 5:1, with the difference in labeling ratios on somata vs. myelin directly attributable to the greater number of very small gap junctions on myelin that were labeled primarily or exclusively for Cx47.

By FRIL, Cx47-containing gap junctions were more abundant on the outer surface of myelin than at all other locations (Table 2 and Fig. 11). Because the fracturing process preferentially produces disproportionately large expanses of flattened membrane surfaces, particularly in the broad expanses of myelin (Rash et al., 1997), FRIL facilitates positive identification and selective examination of heterologous gap junctions on those surfaces. The three major membrane areas having heterologous gap junctions had substantially different fractions of gap junctions that were labeled exclusively for Cx32 (23% in somata and dendrites and 13% for those on the outer surface of myelin) vs. junctions labeled exclusively for Cx47 (31% in somata and dendrites and 66% for those on the outer surface of myelin; Table 2 and Fig. 11, left panel).

Gap junctions on myelin (as in Fig. 5) were much smaller than most gap junctions on oligodendrocyte somata and dendrites (as in Fig. 3 and Fig. 4). However, the total number of connexons and total number of immunogold beads in gap junctions on the outer surface of myelin (56 gap junctions consisting of ca. 4760 connexons labeled by 290 gold beads; LE=1:16) were approximately equal to the number of connexons and gold beads in the fewer and larger gap junctions in somatic and dendritic plasma membranes (13 gap junctions consisting of ca. 4410 connexons and labeled by 232 gold beads; LE=1:19, Table 2 and Fig. 11). On average, somatic and dendritic gap junctions had 4.3 times as many connexons as those on myelin. Moreover, these quantitative FRIL data are consistent with immunofluorescence images (Fig. 1). Notwithstanding species differences in rat vs. mouse white matter, the minute gap junctions on myelin detected by FRIL may account for difficulty in detecting Cx47 immunofluorescence along myelinated fibers in gray matter of mouse and rat brain, and in white matter of mouse brain (Li et al., 2004; present results), consistent with a size/labeling threshold for reliable immunofluorescence detection (Meier et al., 2004). Despite their great abundance, the small size of these junctions also may have precluded their detection by TEM as classically-defined heptalaminar appositions.

In contrast to all heterologous gap junctions, Cx32 was present without detectable Cx47 in three autologous gap junctions between internodal myelin layers at Schmidt-Lanterman incisures (Table 2 and Fig. 11; data from Fig. 7). Likewise, in two samples that were double labeled for Cx29+Cx32 (as part of a separate study; Sik et al., in preparation), limited but unmistakable immunogold labeling for Cx32 was found without labeling for Cx29 in three small (20, 38, and 16 connexons) autologous string gap junctions between successive paranodal loops of myelin (Table 2 and Fig. 11, right panel; data from Fig. 8). Thus, immunogold labeling for Cx32 on ultrastructurally-defined gap junctions within paranodes is consistent with immunofluorescence confocal images showing Cx32 puncta within presumed paranodes (Fig. 6). Moreover, despite the low number of labels (one, one, and five gold beads), the high signal-to-noise ratio (Rash and Yasumura, 1999), moderate LE (ca. 1:30 for 12 nm gold beads, and 1:3 for 6 nm gold beads; see Experimental Procedures for details) and high visibility of immunogold beads has revealed the only three gap junctions yet visualized linking successive paranodal loops in either CNS or peripheral nervous system (PNS) myelin, thereby attesting to the value of FRIL in detecting rare and/or small gap junctions.

DISCUSSION

The locations and relative abundance of Cx32 and Cx47 were defined in ultrastructurally-identified gap junctions in six of seven primary subcellular compartments of oligodendrocytes (shown diagrammatically in Fig. 12A): *heterologous* O/A gap junctions on somata, cytoplasmic processes, outer surfaces of myelin, and everted paranodal loops; and *autologous* gap junctions in Schmidt-Lanterman incisures and between paranodal loops of myelin. No gap junctions were found within compact myelin. These are the first ultrastructural demonstrations of autologous or reflexive gap junctions in paranodes and Schmidt-Lanterman incisures in CNS myelin, first documentation of Cx32 in those gap junctions, and the first ultrastructural evidence for differential distribution of Cx47 vs. Cx32 within different classes of gap junctions in different subcellular locations of oligodendrocytes.

Relative amounts of Cx47 vs. Cx32

Immunofluorescence labeling for Cx47 was more intense than for Cx32 on oligodendrocyte somata in white matter; and by FRIL, immunogold labeling for Cx47 was several times as abundant as for Cx32 at heterologous O/A gap junctions. With Cx32 but not Cx47 demonstrated in *autologous* gap junctions in the same replicas, these data suggest that Cx47 (rather than Cx32) is the predominant connexin at heterologous O/A gap junctions, whereas Cx32 is the predominant or sole connexin at autologous gap junctions. Moreover, the approximately equal number of connexons on the outer surface of myelin as compared with the number of connexons in all other oligodendrocyte locations (Fig. 11) suggests that the abundant but minute gap junctions on myelin contribute substantially to O/A coupling.

Connexin coupling partners and subcellular pathways for gap junctional communication

Lack of permissive coupling of oligodendrocyte Cx32 with astrocyte Cx43 (White and Bruzzone, 1996) and much greater amounts of Cx43 vs. Cx32 in the same O/A junctions (Rash et al., 2001) suggested that an additional but abundant oligodendrocyte connexin was yet to be identified. Identification of Cx47 as this abundant oligodendrocyte connexin is supported by demonstration of equivalent amounts and nearly precise co-localizations of oligodendrocyte Cx47 with astrocyte Cx43 (Odermatt et al., 2003; Li et al., 2004; Altevogt and Paul, 2004; this report). The less abundant oligodendrocyte Cx32 appears to couple with astrocyte Cx30 (and possibly Cx26) (Nagy et al., 2003b). In addition, paucity of Cx29 in oligodendrocyte somata (Nagy et al., 2003a), apparent absence of Cx29 in O/A gap junctions (Sik et al., unpublished observations), and current results suggest that Cx47 and Cx32 are the primary or sole connexins in the oligodendrocyte side of O/A junctions. Because astrocytes extensively couple with oligodendrocytes (Sandri et al., 1977; Waxman and Black, 1984; Mugnaini, 1986; Rash et al., 1997, 2001; Rios et al., 2003), the presence of abundant gap junctions on the four major cytoplasmic regions of oligodendrocytes (this report) implies huge and vital gap junctional coupling capacity for delivery, removal and general flow of ions, osmotic water and metabolites that sustain normal functioning of oligodendrocytes.

Immunofluorescence for Cx32 at paranodes and Schmidt-Lanterman incisures in PNS, and evidence for radial movement of substances across myelin suggested the existence and functional roles of gap junctions at Schmidt-Lanterman incisures and between paranodal loops in PNS (Balice-Gordon et al., 1998; Arroyo and Scherer, 2000). Cx32-containing gap junctions were recently confirmed by FRIL in incisures of PNS myelin (Meier et al., 2004). FRIL now reveals Cx32 in ultrastructurally-defined gap junctions of paranodes and Schmidt-Lanterman incisures in CNS myelin. The apparent absence of Cx47 and Cx29 at these same locations suggests that these autologous gap junctions are homotypic for Cx32. Different conductance or regulatory properties and different targeting mechanisms for Cx32 may underlie presence of Cx32 and apparent exclusion of Cx29 and Cx47 at these intracellular sites. Although Cx32

forms homotypic reflexive O/O gap junctions, it appears incapable of forming intercellular O/O gap junctions, suggesting that permissiveness of coupling is not the only factor involved in regulating oligodendrocyte intercellular coupling.

Possible roles for paranodal gap junctions in modulating saltatory conduction

Myelin sheaths, their complex intercellular appositions with axons at paranodes, their molecular specializations at juxtaparanodal membranes, and their intercellular gap junctional couplings with astrocytes are far more complex structurally, functionally, and compositionally than presumed only five years ago. For example, caspr KO mice lose paranodal septate junctions, have disrupted localization of K^+ channels (Rios et al., 2003), and saltatory conduction is disrupted, suggesting an essential role for high transparanodal electrical resistance in facilitating saltatory conduction. In addition, caspr-containing septate junctions create overlapping double-spirals of thin, electrically-isolated compartments (paranodal cytoplasm and paranodal extracellular space) that are structurally analogous to the spirally-wound layers of electrolytic capacitors. Cx32-containing gap junctions between successive paranodal loops (this report) may provide pathways for regulating electrical resistance across paranodes, regulating transparanodal electrical capacitance, and possibly for creating and collapsing incremental transparanodal voltage steps between paranodal layers (see below).

Primary source of potassium in “potassium siphoning”

Astrocyte endfeet have high “specific conductance” for K^+ (Newman, 1986), and particularly large K^+ fluxes were measured across astrocyte endfeet following high axonal activity (Orkand et al., 1966; Newman, 1986). Thus, astrocyte endfeet were suggested to represent the endpoint in a proposed process called “potassium siphoning” or “potassium spatial buffering” in the CNS (Orkand et al., 1966; Newman, 1986; Kofuji and Newman, 2004). However, the requisite pathway for K^+ movement *into* astrocytes was entirely unknown. As a consequence, axonal K^+ efflux during saltatory conduction was initially proposed to occur across the axonal plasma membrane at nodes of Ranvier, directly into surrounding astrocyte “fingers” (Waxman and Black, 1984), thereby apparently accounting for the source of ions and water in the first structural model of potassium siphoning. Based on assumptions of the passive nature of myelin, oligodendrocytes were presumed not to be directly involved in potassium homeostasis. However, compelling recent experiments have revealed that voltage-gated K^+ efflux does *not* occur at mammalian nodes of Ranvier. Instead, K^+ efflux occurs almost exclusively across the “juxtaparanodal” axolemma in the area that is completely enclosed *within* myelin sheaths (David et al., 1992, 1993; Arroyo and Scherer, 2000; Chiu, 2005; reviewed by Rasband, 2004), with paranodal tight junctions restricting diffusion of K^+ into the surrounding CNS parenchyma.

In juxtaparanodal regions beneath myelin, each axonal depolarization transiently raises “periaxonal” potassium from 2 mM to 20–100 mM (David et al., 1992). Initially, this high extracellular potassium concentration severely alters axonal electrical properties (Goldman, 1943; Hodgkin and Huxley, 1952) by producing both an intra-axonal “prolonged negative potential” and a strong K^+ depolarization (up to +78 mV; average=+40 mV), as measured in the “peri-internodal” compartment (David et al., 1992; also Chiu, 2005). (At that time, the peri-internodal compartment was not identifiable as either extra-axonal space or as the innermost cytoplasmic layer of myelin; G. David, personal communication). More recently, high K^+ conductance into the innermost cytoplasmic layer of myelin was found to occur via a variety of “inward rectifying” and voltage-gated K^+ channels, and via K^+ “leak” channels localized to the juxtaparanodal membranes of both CNS and PNS myelin (Söhl and Willecke, 2003; Clarke et al., 2004; Kalsi et al., 2004; reviewed by Olsen and Sontheimer, 2005). Influx of K^+ through these ion channels into internodal myelin would account for the prolonged +36 mV to +74 mV depolarization of the peri-internodal compartment following each axonal action

potential (David et al., 1992). This transient intracellular potassium concentration (Fig. 12B), combined with the high electrical potential difference (+120 to +159 mV) with respect to the coupled astrocyte syncytium (nominally −85 mV) would provide a strong electrochemical driving force for potassium siphoning, from innermost myelin to the electrically-coupled astrocyte syncytium. Although some of the excess K^+ in the innermost layer of myelin is presumed to return to the periaxonal space for subsequent return to the axon (David et al., 1992), we propose that much is transported to the external layer of myelin via two convergent pathways (Fig. 12): 1) circumferential cytoplasmic diffusion via the spiral cytoplasmic loops of myelin at paranodes and incisures, or 2) more direct *radial* diffusion to the outer layer by way of Cx32-containing gap junctions in both paranodes and incisures (Balice-Gordon et al., 1998). From outer cytoplasmic myelin, K^+ and associated osmotic water are proposed to be transported through abundant O/A gap junctions into the astrocyte syncytium, presumably augmented by the high osmotic concentration and by the +120 to +150 mV electrical potential difference between innermost myelin and the coupled astrocytes, as diagrammed in Fig. 12B.

A role for Cx32/Cx47 gap junctional pathways in “potassium siphoning”

Cx32 is present in both PNS and CNS myelin, whereas Cx47 is present only in CNS myelin. Alteration or deletion of Cx32 results in grossly distended innermost layers of myelin in mouse *PNS* (Anzini et al., 1997) and similar swelling of myelin in X-linked Charcot-Marie-Tooth disease (CMTX) in humans (Bergoffen et al., 1993), both of which are consistent with disruption of gap junction pathways for osmotic and ionic homeostasis in PNS myelin. However, virtual absence of myelin disruptions in *CNS* of Cx32 KO mice (Scherer et al., 1998) suggests that the continued presence of Cx47-containing gap junctions in these KO animals (Nagy et al., 2003b) minimizes Cx32 KO-induced damage to CNS myelin. In contrast, Cx47 KO mice had substantial swelling of cytoplasmic myelin in CNS (Menichella et al., 2003; Odermatt et al., 2003), suggesting that continued presence of less abundant Cx32 at O/A gap junctions in Cx47 KO mice was unable to compensate fully for loss of the more abundant Cx47 normally at O/A gap junctions on myelin surfaces. Cx32/Cx47 double-KO mice had even greater structural and physiological defects (Menichella et al., 2003), including gross swelling of innermost and outermost myelin layers, implying disruption of normal pathways for removal of excess water and ions and/or disruption of pathways for metabolite exchange between oligodendrocytes and astrocytes. This was first suggested by Menichella et al. (2003) to be a major factor underlying destruction of myelin in Cx32/Cx47 double-KO mice.

The newly-discovered Cx32 and Cx47 gap junctions within myelin and linking myelin with astrocytes may represent the long-sought structural pathway required in long-distance “potassium siphoning” or “potassium spatial buffering” (Orkand et al., 1966; Newman, 1986; Kofuji and Newman, 2004). In light of the above, absence of both Cx32 and Cx47 in double-KO mice would eliminate all intercellular pathways for potassium siphoning from myelin, presumably causing the buildup of axonally-derived potassium and osmotic water within myelin and the observed swelling of both the inner and outer cytoplasmic myelin layers (Menichella et al., 2003; Odermatt et al., 2003). This model for osmotic- and voltage-augmented “dynamic potassium siphoning” from the innermost layer of myelin to astrocyte endfeet is now directly testable because the swollen innermost cytoplasmic layer of CNS myelin in Cx47 KO mice should facilitate insertion of K^+-selective electrodes, thereby allowing direct measurement of proposed K^+ currents into myelin during saltatory conduction in the CNS.

Acknowledgements

Funded by grants from CIHR (A.S. and J.I.N.), the Savoy Foundation (A.S.), and NIH (NS44010, NS44395, and NS38121; J.E.R.). We thank B. McLean, N. Nolette, O. Szalay and P. Lemieux for excellent technical assistance, and Aaron Magnie and Jennifer Sampson for preparation of stereoscopic FRIL images.

References

Altevogt BM, Paul DL. Four classes of intercellular channels between glial cells in the CNS. J Neurosci 2004;24:4313–4323. [PubMed: 15128845]

Anzini P, Neuberg DHH, Schachner M, Nelles E, Willecke K, Zielasek J, Toyka KV, Suter U, Martini R. Structural abnormalities and deficient maintenance of peripheral nerve myelin in mice lacking the gap junction protein connexin 32. J Neurosci 1997;17:4545–4551. [PubMed: 9169515]

Arroyo EJ, Scherer SS. On the molecular architecture of myelinated fibers. Histochem Cell Biol 2000;113:1–18. [PubMed: 10664064]

Bahr M, Andres F, Timmerman V, Nelis ME, Van Broeckhoven C, Dichgans J. Central visual, acoustic, and motor pathway involvement in a Charcot-Marie-Tooth family with an Asn205Ser mutation in the connexin 32 gene. J Neurol Neurosurg Psychiatry 1999;66:202–206. [PubMed: 10071100]

Balice-Gordon RJ, Bone LJ, Scherer SS. Functional gap junctions in the Schwann cell myelin sheath. J Cell Biol 1998;142:1095–1104. [PubMed: 9722620]

Bergoffen J, Scherer SS, Wang S, Oronzi-Scott M, Paul D, Chen K, Lensch MW, Chance P, Fischbeck K. Connexin mutations in X-linked Charcot-Marie-Tooth disease. Science 1993;262:2039–2042. [PubMed: 8266101]

Black JA, Waxman SG. The perinodal astrocyte. Glia 1988;1:169–183. [PubMed: 2976037]

Bruzzone R, Goodenough DA. Gap junctions: ductin or connexins: which component is the critical one? Bioessays 1995;17:744. [PubMed: 7661855]

Chiu SY. Functions and distribution of voltage-gated sodium and potassium channels in mammalian Schwann cells. Glia 2005;4:541–558. [PubMed: 1720761]

Clarke CE, Veale EL, Green PJ, Meadows HJ, Mathie A. Selective block of the human 2-P domain potassium channel, TASK-3, and the native leak potassium current, IKSO, by zinc. J Physiol (Lond) 2004;560:51–62. [PubMed: 15284350]

Condorelli DF, Trovato-Salinaro A, Mudo A, Mirone MB, Belluardo N. Cellular expression of connexins in the rat brain: neuronal localization, effects of kainate-induced seizures and expression in apoptotic neuronal cells. Eur J Neurosci 2003;18:1807–1827. [PubMed: 14622215]

Coppen SR, Kaba RA, Halliday D, Dupont E, Skepper JN, Elneil S, Severs NJ. Comparison of connexin expression patterns in the developing mouse heart and human foetal heart. Mol Cell Biochem 2003;242:121–127. [PubMed: 12619874]

David G, Barrett JN, Barrett EF. Evidence that action potentials activate an internodal potassium conductance in lizard myelinated axons. J Physiol 1992;445:277–301. [PubMed: 1501136]

David G, Barrett JN, Barrett EF. Activation of internodal potassium conductance in rat myelinated axons. J Physiol 1993;472:177–202. [PubMed: 8145140]

Dere E, De Sousa-Silva MA, Frisch C, Teubner B, Sohl G, Willecke K, Huston JP. Connexin30-deficient mice show increased emotionality and decreased rearing activity in the open-field along with neurochemical changes. Eur J Neurosci 2003;18:629–638. [PubMed: 12911759]

Einheber S, Zanazzi G, Ching W, Scherer S, Milner TA, Peles E, Salzer JL. The axonal membrane protein Caspr, a homologue of neurexin IV, is a component of the septate-like paranodal junctions that assemble during myelination. J Cell Biol 1997;139:1495–1506. [PubMed: 9396755]

Filippov MA, Hormuzdi S, Fuchs EC, Monyer H. A reporter allele for investigating connexin 26 gene expression in the mouse brain. Eur J Neurosci 2003;18:3183–3192. [PubMed: 14686892]

Goldman DE. Potential, impedance, and rectification in membranes. J Gen Physiol 1943;27:37–60.

Goodenough DA, Goliger JA, Paul DL. Connexins, connexons and intercellular communication. Annu Rev Biochem 1996;65:475–502. [PubMed: 8811187]

Hibino H, Fujita A, Iwai K, Yamada M, Kurachi Y. Differential assembly of inwardly rectifying K+ channel subunits, Kir4.1 and Kir5.1, in brain astrocytes. J Biol Chem 2004;279:44065–44073. [PubMed: 15310750]

Hodgkin AL, Huxley AF. A quantitative description of membrane current and its application to conduction and excitation in nerve. J Physiol 1952;117:500–544. [PubMed: 12991237]

Itoh M, Furuse M, Morita K, Kubota K, Saitou M, Tsukita SH. Direct binding of three tight junction-associated MAGUKs, ZO-1, ZO-2, and ZO-3, with the COOH termini of claudins. J Cell Biol 1999;147:1351–1363. [PubMed: 10601346]

Kalsi AS, Greenwood K, Wilkin G, Butt AM. Kir4.1 expression by astrocytes and oligodendrocytes in CNS white matter: a developmental study in the rat optic nerve. J Anat 2004;204:475–485. [PubMed: 15198689]

Kleopas KA, Orthmann JL, Enriquez A, Paul DL, Scherer SS. Unique distributions of the gap junction proteins connexin29, connexin32, and connexin47 in oligodendrocytes. Glia 2004;47:346–357. [PubMed: 15293232]

Kofuji P, Newman EA. Potassium buffering in the central nervous system. Neuroscience 2004;129:1043–1054.

Kunzelmann P, Schroder W, Traub O, Steinhauser C, Dermietzel R, Willecke K. Late onset and increasing expression of the gap junction protein connexin30 in adult murine brain and long-term cultured astrocytes. Glia 1999;25:111–119. [PubMed: 9890626]

Li J, Hertzberg EL, Nagy JI. Connexin32 in oligodendrocytes and association with myelinated fibers in mouse and rat brain. J Comp Neurol 1997;379:571–591. [PubMed: 9067844]

Li X, Ionescu A-V, Lynn BD, Lu S, Kamasawa N, Morita M, Davidson KGV, Yasumura T, Rash JE, Nagy JI. Connexin47, connexin29 and connexin32 co-expression in oligodendrocytes and Cx47 association with zonula occludens-1 (ZO-1) in mouse brain. Neuroscience 2004;126:611–630. [PubMed: 15183511]

Li X, Lynn BD, Olson C, Meier C, Davidson KGV, Yasumura T, Rash JE, Nagy JI. Connexin29 expression, immunocytochemistry and freeze-fracture replica immunogold labeling (FRIL) in sciatic nerve. Eur J Neurosci 2002;16:795–806. [PubMed: 12372015]

Massa PT, Mugnaini E. Cell junctions and intramembrane particles of astrocytes and oligodendrocytes: a freeze-fracture study. Neuroscience 1982;7:523–538. [PubMed: 7078735]

Meier C, Dermietzel R, Davidson KGV, Yasumura T, Rash JE. Connexin32-containing gap junctions in Schwann cells at the internodal zone of partial myelin compaction and in Schmidt-Lanterman incisures. J Neurosci 2004;24:3186–3198. [PubMed: 15056698]

Menichella DM, Goodenough DA, Sirkowski E, Scherer SS, Paul DL. Connexins are critical for normal myelination in the CNS. J Neurosci 2003;23:5963–5973. [PubMed: 12843301]

Mercier F, Hatton GI. Connexin 26 and basic fibroblast growth factor are expressed primarily in the subpial and subependymal layers in adult brain parenchyma: Roles in stem cell proliferation and morphological plasticity? J Comp Neurol 2001;431:88–104. [PubMed: 11169992]

Mugnaini E (1986) Cell junctions of astrocytes, ependyma, and related cells in the mammalian central nervous system, with emphasis on the hypothesis of a generalized functional syncytium of supporting cells. In: Astrocytes. Vol. 1 (Fedoroff S, Vernadakis A, eds), pp 329–371. New York: Academic Press.

Mugnaini E, Osen KK, Schnapp B, Friedrich VL Jr. Distribution of Schwann cell cytoplasm and plasmalemmal vesicles (caveolae) in peripheral myelin sheaths. An electron microscopic study with thin sections and freeze-fracturing. J Neurocytol 1977;6:647–668. [PubMed: 599372]

Nagy JI, Dudek FE, Rash JE. Update on connexins and gap junctions in neurons and glia in the mammalian central nervous system. Brain Res Brain Res Rev 2004;47:191–215. [PubMed: 15572172]

Nagy JI, Ionescu A-V, Lynn BD, Rash JE. Connexin29 and connexin32 at oligodendrocyte and astrocyte gap junctions and in myelin of the mouse central nervous system. J Comp Neurol 2003a;464:356–370. [PubMed: 12900929]

Nagy JI, Ionescu A-V, Lynn BD, Rash JE. Coupling of astrocyte connexins Cx26, Cx30, Cx43 to oligodendrocyte Cx29, Cx32, Cx47: Implications from normal and connexin32 knockout mice. Glia 2003b;44:205–218. [PubMed: 14603462]

Nagy JI, Li X, Rempel J, Stelmack GL, Patel D, Staines WA, Yasumura T, Rash JE. Connexin26 in adult rodent CNS: demonstration at astrocytic gap junctions and co-localization with connexin30 and connexin43. J Comp Neurol 2001;441:302–323. [PubMed: 11745652]

Nagy JI, Rash JE. Connexins and gap junctions of astrocytes and oligodendrocytes in the CNS. Brain Res Rev 2000;32:29–44. [PubMed: 10751655]

Nagy JI, Rash JE. Astrocyte and oligodendrocyte connexins of the glial syncytium in relation to astrocyte anatomical domains and spatial buffering. Cell Commun Adhes 2003;10:401–406. [PubMed: 14681048]

Newman EA. High potassium conductance in astrocyte endfeet. Science 1986;233:453–454. [PubMed: 3726539]

Nielsen S, Nagelhus EA, Amiry-Moghaddam M, Bourque C, Agre P, Ottersen OP. Specialized membrane domains for water transport in glial cells: High-resolution immunogold cytochemistry of aquaporin-4 in rat brain. J Neurosci 1997;17:171–180. [PubMed: 8987746]

Ochalski PAY, Frankenstein UN, Hertzberg EL, Nagy JI. Connexin43 in rat spinal cord: localization in astrocytes and identification of heterotypic astro-oligodendrocytic gap junctions. Neuroscience 1997;76:931–945. [PubMed: 9135062]

Odermatt B, Wellershaus K, Wallraff A, Seifert G, Degen J, Euwens C, Fuss B, Bussow H, Schilling K, Steinhauser C, Willecke K. Connexin 47 (Cx47)-deficient mice with enhanced green fluorescent protein reporter gene reveal predominant oligodendrocytic expression of Cx47 and display vacuolized myelin in the CNS. J Neurosci 2003;23:4549–4559. [PubMed: 12805295]

Olsen ML, Sontheimer H (2005) Voltage-activated ion channels in glial cells. In: Neuroglia (Kettenmann H, Ransom BR, eds), pp 112–130. New York: Oxford University Press.

Orkand RK, Nicholls JG, Kuffler SW. Effect of nerve impulses on the membrane potential of glial cells in the central nervous system of amphibia. J Neurophysiol 1966;29:788–806. [PubMed: 5966435]

Peles E, Nativ M, Lustig M, Grumet M, Schilling J, Martinez R, Plowman GD, Schlessinger J. Identification of a novel contactin-associated transmembrane receptor with multiple domains implicated in protein-protein interactions. EMBO J 2005;16:978–988. [PubMed: 9118959]

Pereda A, O'Brien J, Nagy JI, Bukauskas F, Davidson KGV, Kamasawa N, Yasumura T, Rash JE. Connexin35 mediates electrical transmission at mixed synapses on Mauthner cells. J Neurosci 2003;23:7489–7503. [PubMed: 12930787]

Rasband MN. It's "juxta" potassium channel! J Neurosci Res 2004;76:749–757. [PubMed: 15160387]

Rash JE, Davidson KGV, Yasumura T, Furman CS. Freeze-fracture and immunogold analysis of aquaporin-4 (AQP4) square arrays, with models of AQP4 lattice assembly. Neuroscience 2004a; 129:915–934. [PubMed: 15561408]

Rash JE, Pereda A, Kamasawa N, Furman CS, Yasumura T, Davidson KGV, Dudek FE, Olson C, Nagy JI. High-resolution proteomic mapping in the vertebrate central nervous system: Close proximity of connexin35 to NMDA glutamate receptor clusters and co-localization of connexin36 with immunoreactivity for zonula occludens protein-1 (ZO-1). J Neurocytol 2004b;33:131–152. [PubMed: 15173637]

Rash JE, Dillman R, Morita M, Whalen LR, Guthrie PB, Fay-Guthrie D, Wheeler DW (1995) Grid-mapped freeze fracture: correlative confocal laser scanning microscopy and freeze-fracture electron microscopy of preselected neurons in spinal cord slices. In: Techniques in modern biomedical microscopy, Vol 2. Rapid freezing, freeze-fracture and deep etching (Shotton DM, Severs NJ, eds), pp 127–150. New York, NY: Wiley-Liss.

Rash JE, Duffy HS, Dudek FE, Bilhartz B, Whalen LR, Yasumura T. Grid-mapped freeze-fracture analysis of gap junctions in gray and white matter of adult rat central nervous system, with evidence for a "panglial syncytium" that is not coupled to neurons. J Comp Neurol 1997;388:265–292. [PubMed: 9368841]

Rash JE, Yasumura T. Direct immunogold labeling of connexins and aquaporin4 in freeze-fracture replicas of liver, brain and spinal cord: factors limiting quantitative analysis. Cell Tissue Res 1999;296:307–321. [PubMed: 10382274]

Rash JE, Yasumura T, Dudek FE, Nagy JI. Cell-specific expression of connexins, and evidence for restricted gap junctional coupling between glial cells and between neurons. J Neurosci 2001;21:1983–2001. [PubMed: 11245683]

Rash JE, Yasumura T, Hudson CS, Agre P, Nielsen S. Direct immunogold labeling of aquaporin-4 in "square arrays" of astrocyte and ependymocyte plasma membranes in rat brain and spinal cord. Proc Natl Acad Sci U S A 1998;95:11981–11986. [PubMed: 9751776]

Raviola E, Gilula NB. Gap junctions between photoreceptor cells in the vertebrate retina. Proc Natl Acad Sci U S A 1973;70:1677–1681. [PubMed: 4198274]

Rios JC, Rubin M, Martin M, Downey RT, Einheber S, Rosenbluth J, Levinson SR, Bhat M, Salzer JL. Paranodal interactions regulate expression of sodium channel subtypes and provide a diffusion barrier for the node of Ranvier. J Neurosci 2003;23:7001–7011. [PubMed: 12904461]

Saitou M, Ando-Akatsuka Y, Itoh M, Furuse M, Nazawa J, Fujimoto K, Tsukita SA. Mammalian occludin in epithelial cells: its expression and subcellular distribution. Eur J Cell Biol 1997;73:222–231. [PubMed: 9243183]

Sandri C, Van Buren JM, Akert K. Membrane morphology of the vertebrate nervous system. Prog Brain Res 1977;46:1–384. [PubMed: 854571]

Satir BH, Satir P (1979) Partitioning of intramembrane particles during the freeze-fracture procedure. In: Freeze fracture: methods, artifacts, and interpretations (Rash JE, Hudson CS, eds), pp 43–49. New York: Raven Press.

Scherer SS, Deschenes SM, Xu Y-T, Grinspan JP, Fischbeck KH, Paul DL. Connexin32 is a myelin-related protein in the PNS and CNS. J Neurosci 1995;15:8281. [PubMed: 8613761]

Scherer SS, Xu YT, Nelles E, Fischbeck K, Willecke K, Bone LJ. Connexin32-null mice develop demyelinating peripheral neuropathy. Glia 1998;24:8–20. [PubMed: 9700485]

Schnapp B, Mugnaini E (1978) Membrane architecture of myelinated fibers as seen by freeze fracture. In: Physiology and patho-biology of axons (Waxman S, ed), pp 83–123. New York: Raven Press.

Severs NJ. Cardiovascular disease. Gap junction-mediated intercellular coupling in health and disease. Novartis Found Symp 1999;219:188–206. [PubMed: 10207905]

Söhl G, Willecke K. An update on connexin genes and their nomenclature in mouse and man. Cell Adhes Commun 2003;10:173–180.

Steere RL. Electron microscopy of structural detail in frozen biological specimens. J Biophys Biochem Cytol 1957;3:45–60. [PubMed: 13416310]

Theis M, Jauch R, Zhuo L, Speidel D, Wallraff A, Doring B, Frisch C, Sohl G, Teubner B, Euwens C, Huston J, Steinhauser C, Messing A, Heinemann U, Willecke K. Accelerated hippocampal spreading depression and enhanced locomotory activity in mice with astrocyte-directed inactivation of connexin43. J Neurosci 2003;23:766–776. [PubMed: 12574405]

Veenstra RD. Size and selectivity of gap junction channels formed from different connexins. J Bioenerg Biomemb 1996;28:327–337.

Waxman SG, Black JA. Freeze-fracture ultrastructure of the perinodal astrocyte and associated glial junctions. Brain Res 1984;308:77–87. [PubMed: 6434150]

White TW, Bruzzone R. Multiple connexin proteins in single intercellular channels: connexin compatibility and functional consequences. J Bioenerg Biomemb 1996;28:339–350.

White TW, Bruzzone R. Gap junctions: fates worse than death? Curr Biol 2000;10:R685–R688. [PubMed: 10996812]

Willecke K, Eiberger J, Degen J, Eckardt D, Romualdi A, Gueldenagel M, Deutsch U, Soehl G. Structural and functional diversity of connexin genes in the mouse and human genome. Biol Chem 2002;383:725–737. [PubMed: 12108537]

Yamamoto T, Ochalski A, Hertzberg EL, Nagy JI. LM and EM immunolocalization of the gap junctional protein connexin 43 in rat brain. Brain Res 1990a;508:313–319. [PubMed: 2155040]

Yamamoto T, Ochalski A, Hertzberg EL, Nagy JI. On the organization of astrocytic gap junctions in the brain as suggested by LM and EM immunocytochemistry of connexin43 expression. J Comp Neurol 1990b;302:853–883. [PubMed: 1964467]

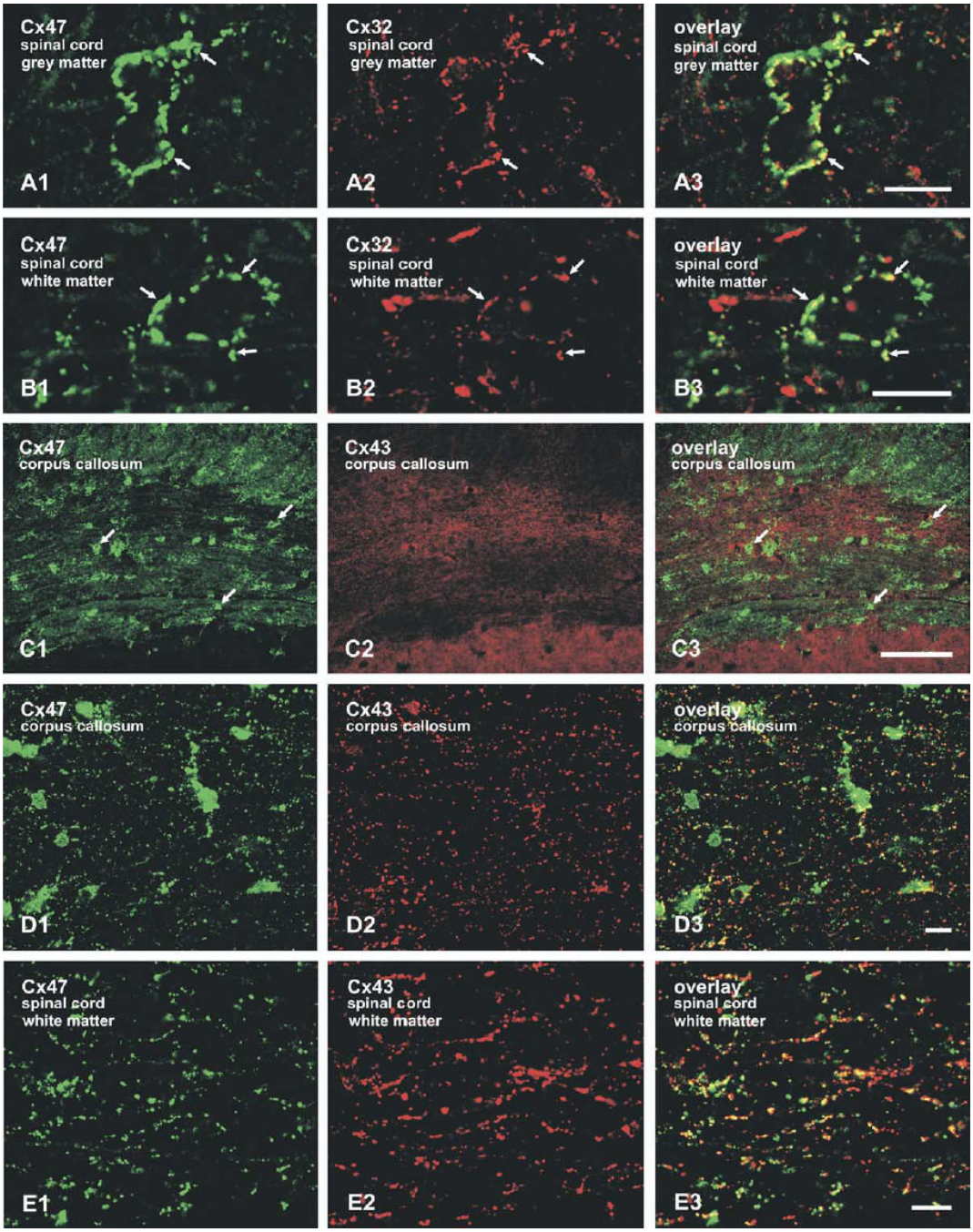

Fig. 1.

Immunofluorescence labeling of oligodendrocyte connexins in gray and white matter of adult rat brain and spinal cord. (A) Confocal double immunofluorescence images of a pair of adjacent oligodendrocyte somata in spinal cord gray matter, showing an abundance of punctate labeling for both Cx47 (A1, arrows) and Cx32 (A2, arrows) around the periphery of the cells. Cx47 and Cx32 are generally co-localized in the overlay (A3, arrows). (B) Confocal double immunofluorescence images of an oligodendrocyte soma in spinal cord white matter, with a relatively greater abundance of punctate labeling for Cx47 (B1, arrows) than for Cx32 (B2, arrows). Co-localization of puncta for Cx47 occurs where Cx32 is also present (B3, arrows). (C) Low magnification micrographs showing oligodendrocyte-associated (arrows) as well as

dispersed punctate labeling of Cx47 and Cx43 in the corpus callosum. (D, E) Confocal double immunofluorescence labeling shows considerable overlap of dispersed Cx47-positive and Cx43-positive puncta in the corpus callosum and spinal cord white matter. Areas of Cx43 (red) without Cx47 presumably represent astrocyte/astrocyte gap junctions. Scale bars=100 μm C; A, B, D, E, 10 μm.

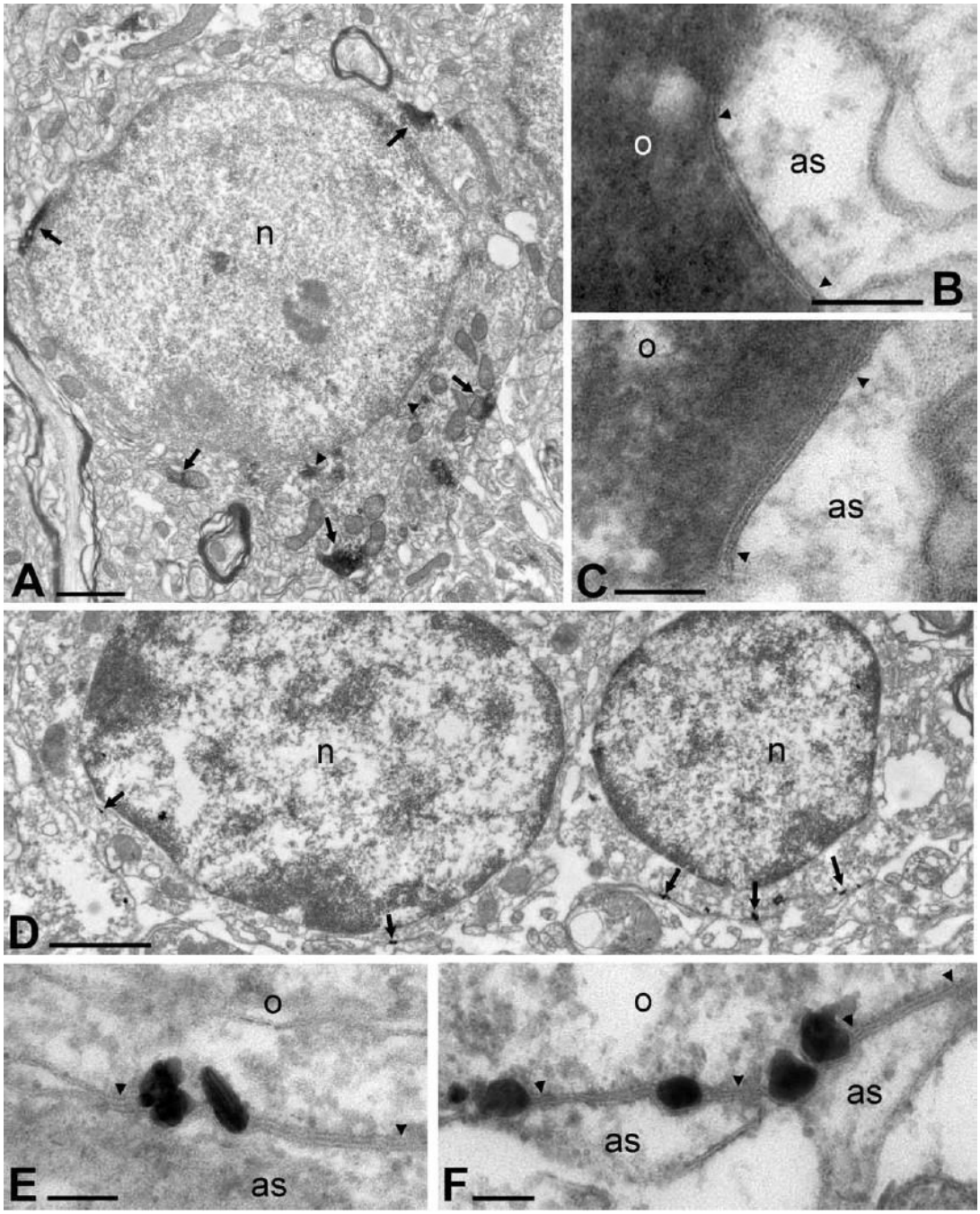

Fig. 2.

Thin-section immunolocalization of Cx47 in adult mouse brain. (A) Oligodendrocyte somata in cerebral cortex immunolabeled with polyclonal anti-Cx47 antibody display large deposits of DAB reaction product in cytoplasmic compartments close to the plasma membrane (arrows), and smaller deposits in the cytoplasm closer to the nucleus (n), associated with presumptive rough endoplasmic reticulum (arrowheads). (B, C) Higher magnifications of DAB deposits near oligodendrocyte (o) plasma membranes in the thalamus (B) and cerebral cortex (C), showing close proximity of deposits to gap junctions (arrowheads) between oligodendrocytes and astrocytes (as), and localization of deposits exclusively on the oligodentrocyte side of junctions. (D) Silver-intensified immunogold labeling showing intracellular sites of Cx47

labeling at plasma membranes of oligodendrocytes (arrows). (E, F) Higher magnification image showing silver-intensified immunolabeling for Cx47 at O/A gap junctions (arrowheads). Scale bars=1 μm A; B, C, 0.1 μm; D, 0.5 μm; E, F, 0.1 μm.

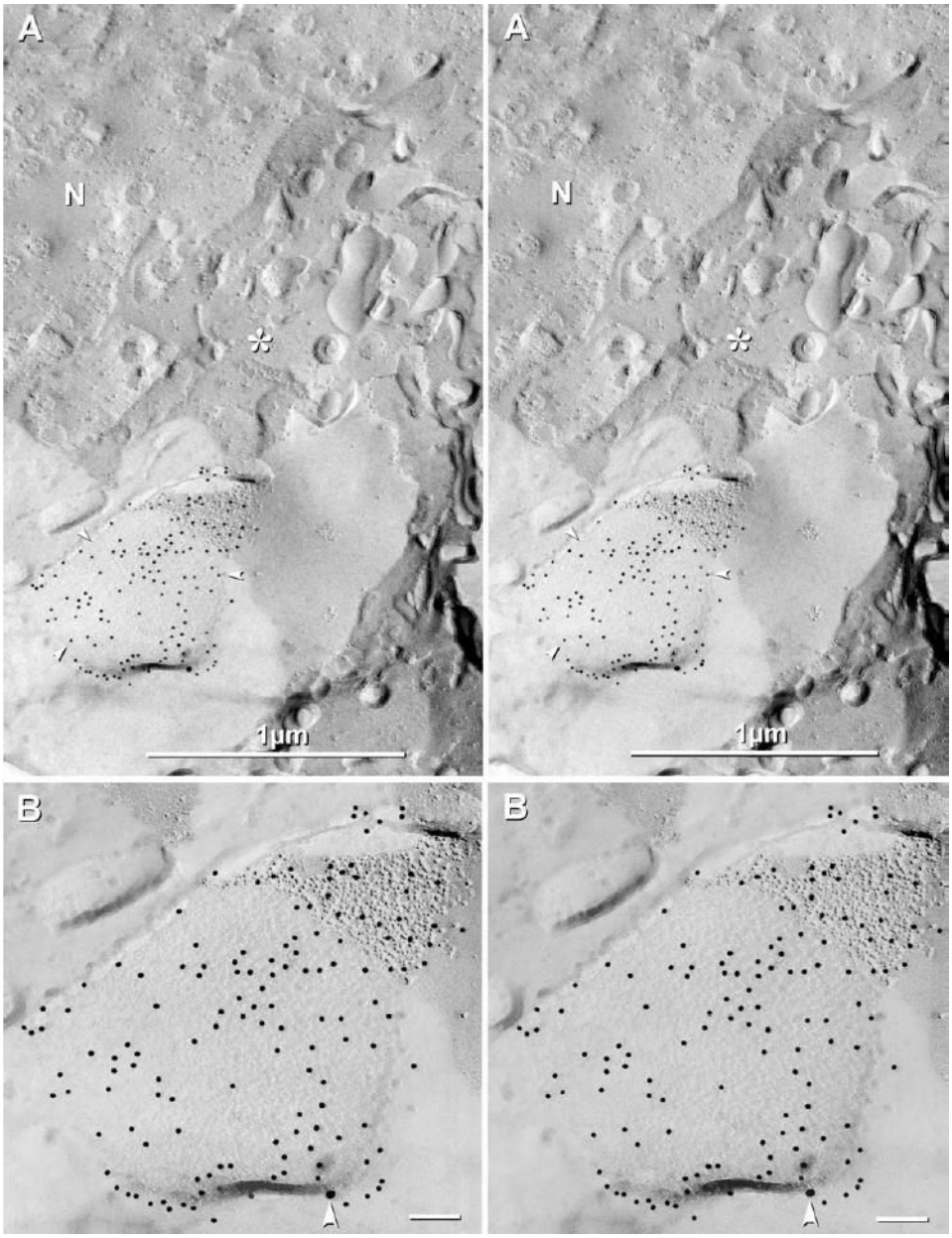

Fig. 3.

Stereoscopic images of gap junctions in oligodendrocyte somatic plasma membranes after double-labeling for Cx47 and Cx32. (A) One large gap junction (three arrowheads delineating its edge) exhibits robust labeling for Cx47 (136 12 nm gold) but little or no labeling for Cx32 (no 6 nm and only one 18 nm gold bead). N, nucleus; *, cytoplasm. The lower left quadrant of the image is not shadowed with platinum because of blockade by a large tissue fragment, but instead is replicated by carbon only. (B) Higher magnification stereoscopic image of the same gap junction. Carbon-replicated connexons are faintly delineated, whereas platinum-shadowed connexons (upper right) are clearly delineated. White arrowhead, 18 nm gold bead for Cx32. Unlabeled scale bars=0.1 μm.

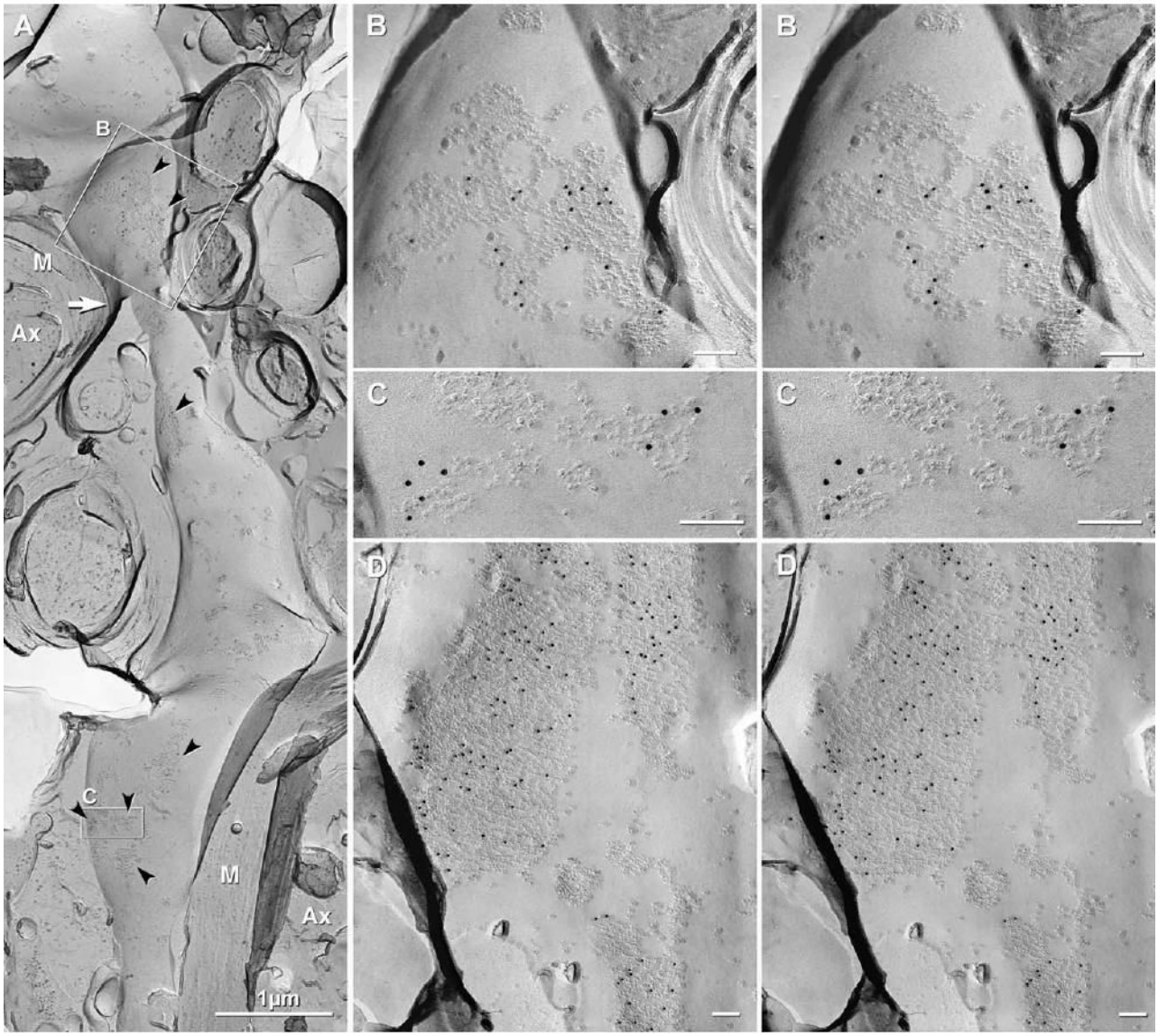

Fig. 4.

Gap junctions on oligodendritic processes in sample of rat spinal cord after single-labeling for Cx47 (12 nm gold beads). (A) Cytoplasmic process (“oligodendrite”) linking an oligodendrocyte soma (not shown) to the outermost layer of myelin (M) of two different cross-fractured axons (Ax). Arrow indicates area of transition from dendritic process to flattened cytoplasmic myelin. Of seven gap junctions on this dendritic process (arrowheads), all were heavily labeled for Cx47. (B) Stereoscopic image of two closely-adjacent gap junctions (or one irregular gap junction), from the inscribed area in 4A; labeled by 20 12 nm gold beads. (C) One or two small gap junctions on the same dendrite; labeled for Cx47 by eight 12 nm gold beads. (D) Large (>1500 connexons), medium and small gap junctions on oligodendrite; labeled for Cx47. Two central “reciprocal patches,” which are composed of mixed IMPs and pits, are not labeled. Unlabeled scale bars=0.1 μm.

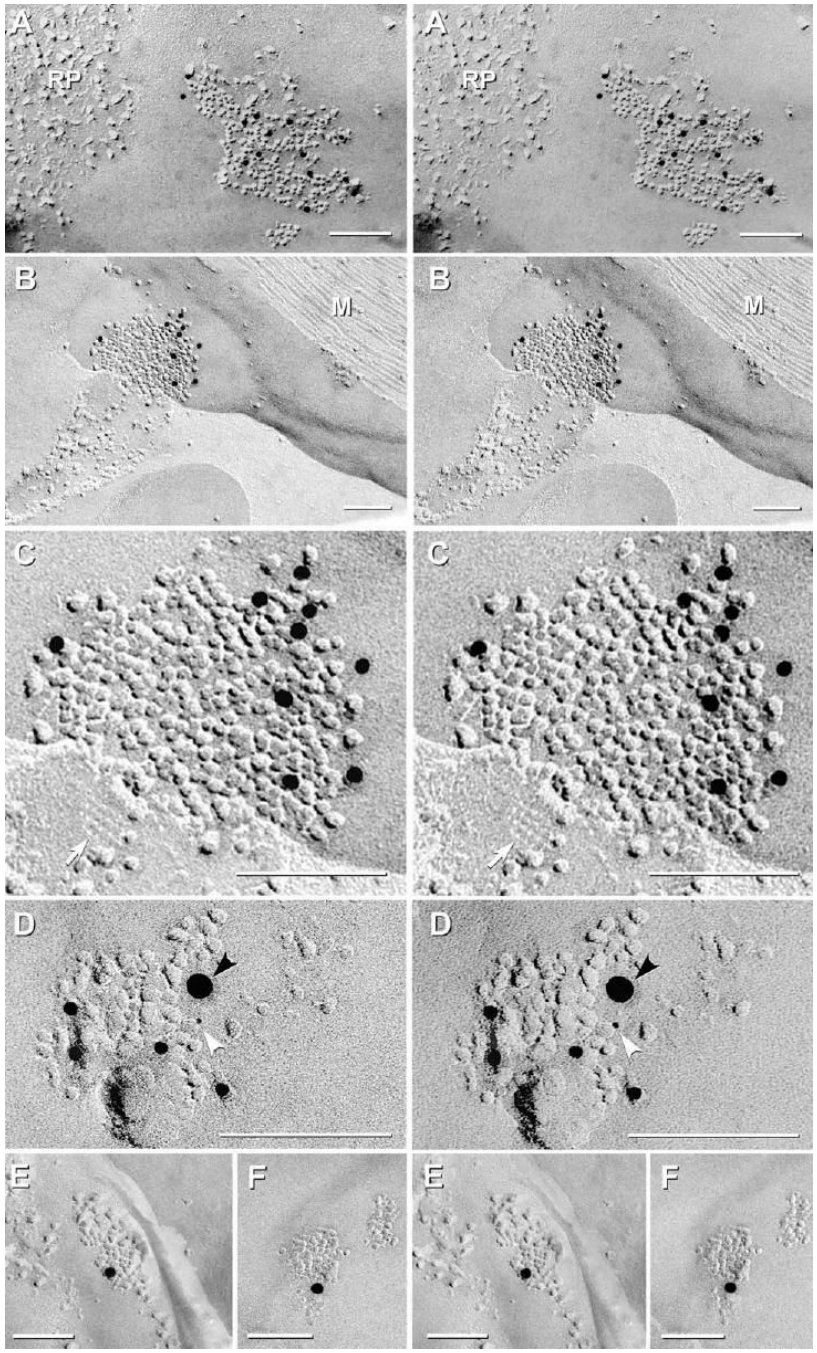

Fig. 5.

Gap junctions on the outer surface of myelin that had been double-labeled for Cx47+Cx32. (A–F) Myelin is characterized by broad expanses of particle free membranes. Gap junctions are distinguished from "reciprocal patches" (RP in A) by having 100% of IMPs on P-faces and 100% of pits on E-faces. Plasma membranes of astrocytes were identified by the presence of E-face images of AQP4 square arrays (C; white arrow). (C) Enlarged image of B. (B) M, cross-fractured myelin. (A–C) Most gap junctions (66%) were immunogold labeled for Cx47 (12 nm gold) but did not label for Cx32. A few (21%), particularly the smallest gap junctions (D), were double-labeled for Cx47 (12 nm gold beads) plus Cx32 (white arrowhead, 6 nm gold

bead; black arrowhead, 18 nm gold bead), and fewer still (13%) on outer myelin (E, F) were labeled for Cx32, only. Scale bars=0.1 μm.

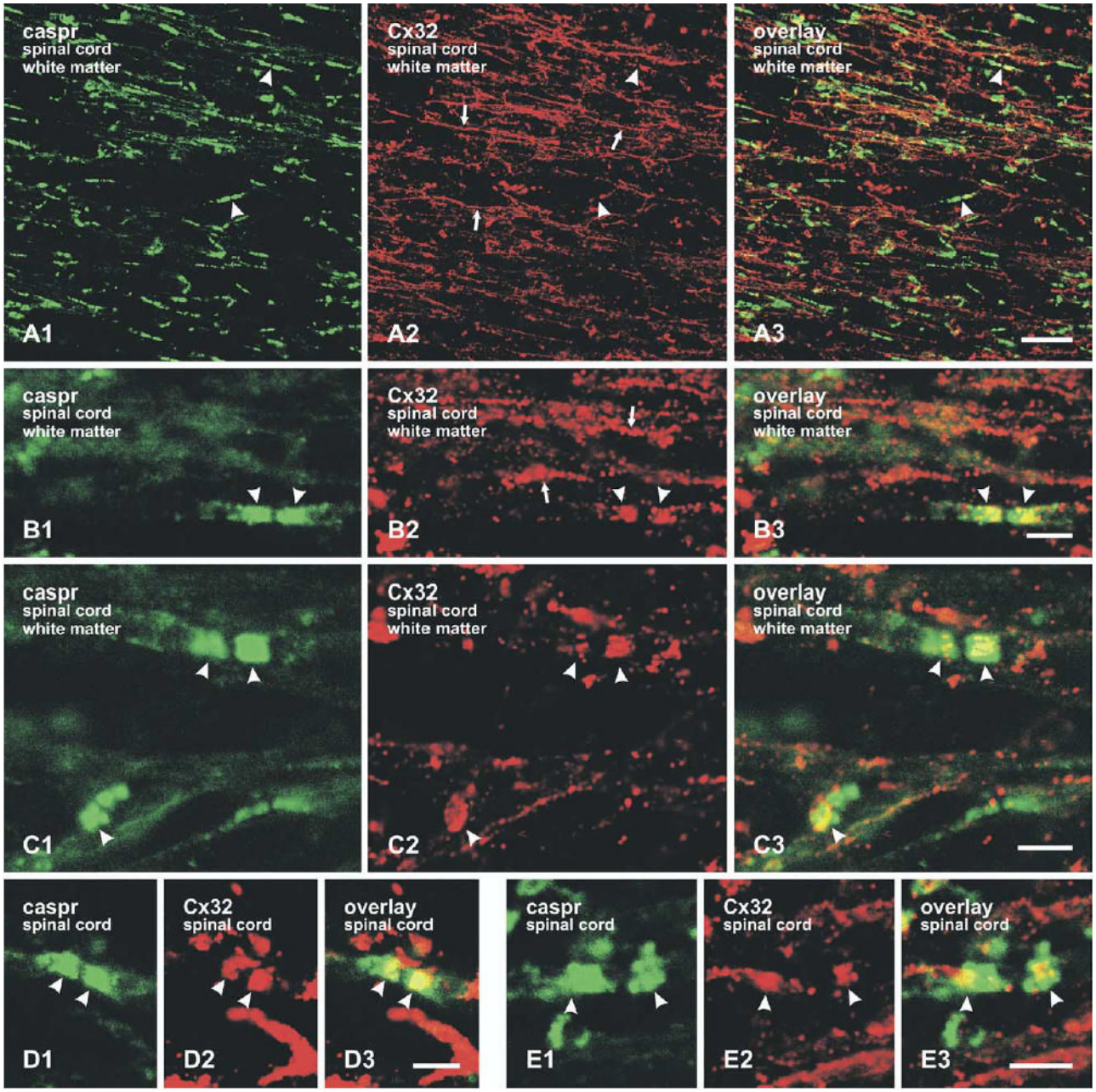

Fig. 6.

Laser scanning confocal double immunofluorescence images of caspr and Cx32 labeling in white matter of adult rat spinal cord. (A) Low magnification images of dorsolateral white matter showing intermittent labeling for caspr along myelinated fibers (A1, arrowheads), intermittent (A2, arrowheads) as well as continuous (A2, arrows) labeling for Cx32 along these fibers, and occasional regions of overlap (A3, arrowheads). (B) Higher magnification images from regions similar to those in (A) showing granular appearance of labeling for Cx32 along some fibers (B2, arrows), and intense immunofluorescence for caspr (B1, arrowheads) and Cx32 (B2, arrowheads) on each side of a node of Ranvier. Overlay shows overlap of labeling (B3, arrowheads). (C–E) Double immunofluorescence labeling showing co-localization of caspr and Cx32 (arrowheads) in other white matter regions of spinal cord, including ventrolateral (C), ventral (D), and dorsal columns (E). Scale bars=25 μm A; B–E, 5 μm.

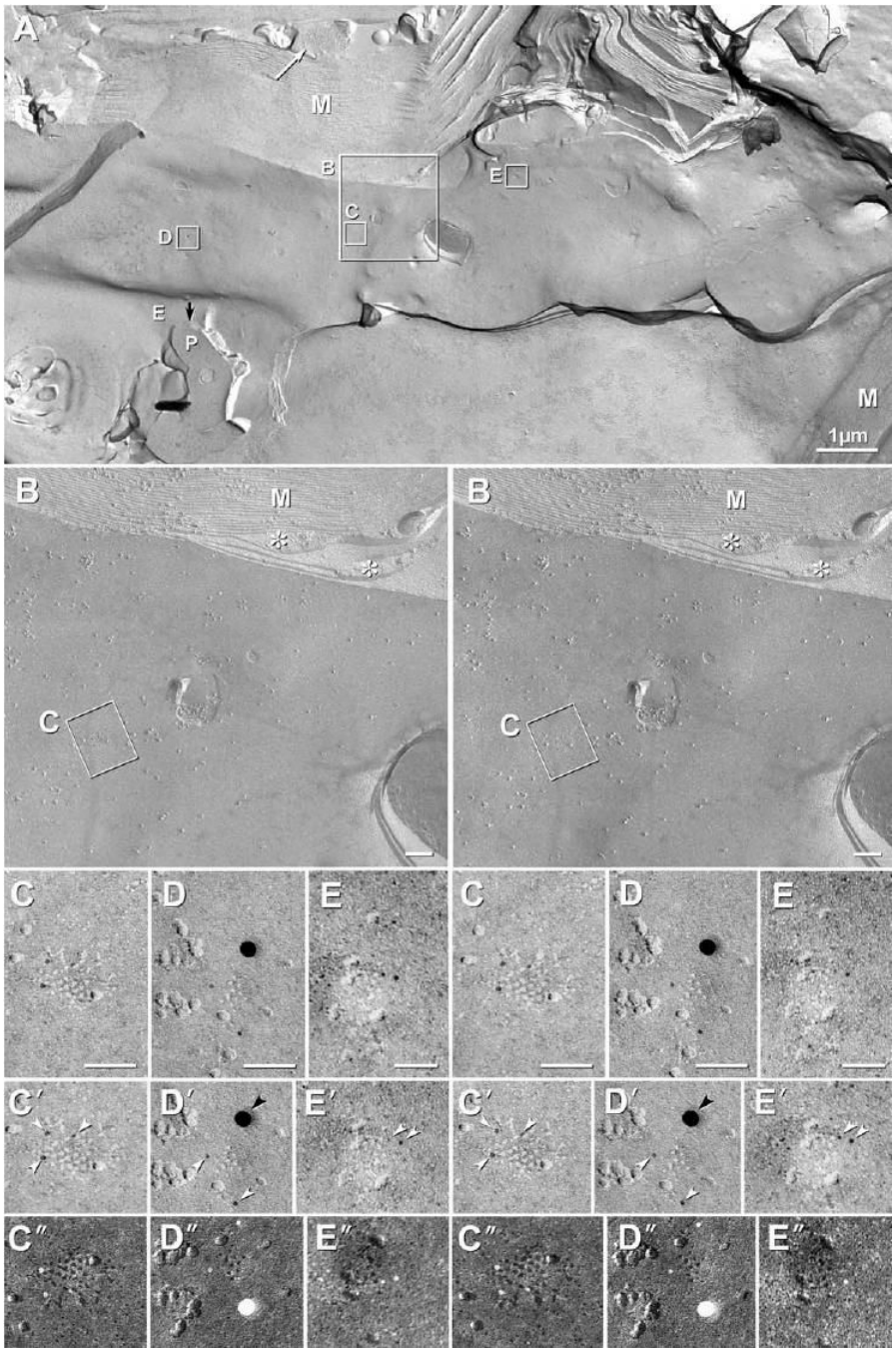

Fig. 7.

FRIL images of gap junctions at Schmidt-Lanterman incisure; between the innermost tongue of cytoplasmic myelin and the second innermost layer of partially-compacted myelin; immunogold labeled for Cx32 (6 nm and 18 nm gold) and Cx47 (12 nm gold, none present). (A) M, myelin; E, E-face; P, P-face; white arrow, astrocyte process containing bundle of GFAP filaments; black arrow, cytoplasm of innermost tongue of myelin. Inscribed areas shown at higher magnification, below. (B) *, cytoplasm of 2nd and 3rd innermost layers of myelin. (C–E) High magnification stereoscopic images of three gap junctions labeled for Cx32 (from small inscribed boxes in A). (C′–E′) Reverse stereoscopic images of C–E allow recognition of 6 nm gold beads against the equally electron-dense platinum replica. White arrowhead, 6 nm gold

beads for Cx32; black arrowhead, 18 nm gold bead for Cx32. (C″–E″) Reversed contrast (i.e. black shadows) versions of C–E, which more clearly reveal the hexagonal arrays of E-face pits (black pits or holes representing where connexons had been removed; black shadows according to the original imaging convention of Steere 1957). Nearby E-face IMPs cast distinctive black shadows, as if the IMPs had been illuminated with white light. However, immunogold beads appear anomalously white. Unlabeled scale bars=0.1 μm.

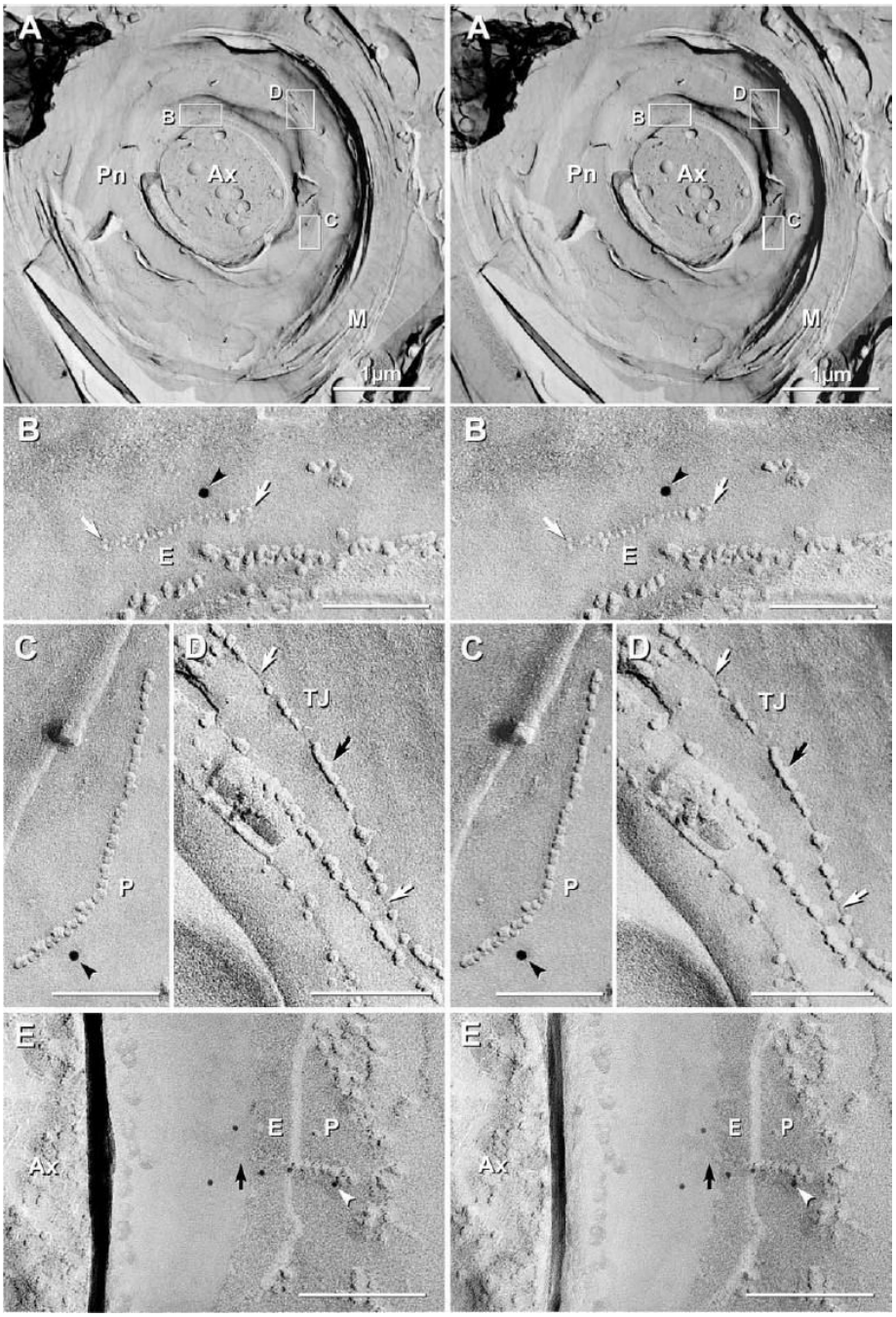

Fig. 8.

Stereoscopic FRIL images of “string” gap junctions linking paranodal loops of myelin after double-labeling for Cx32 (6 and 12 nm) and Cx29 (18 nm; none found in paranodes). (A) In rare cross-fracture through paranodal myelin (M), low magnification images reveal that the outer layers of myelin are compacted, whereas the paranodal loops (Pn) are widely separated and “bowl-shaped,” forming a concave toroidal spiral. (Ax, axon). Inscribed areas shown at higher magnification, below. Within the plasma membrane, two gap junctions (B, C) and several tight junctions (D) are depicted. (B) At higher magnification, linear rows of 20 8 nm E-face pits (E between white arrows) having a center-to-center spacing of 10 nm, and C, 38 9 nm P-face IMPs (P) having center-to-center spacings of 10 nm are labeled for Cx32 by 12 nm

gold beads (black arrowhead), one gold bead in each image, yielding combined labeling efficiencies (Rash and Yasumura, 1999) of ca. LE=1:30. (D) Formaldehyde-fixed tight junctions (TJ) consist of discontinuous rows of partially-fused particles and partially-fused pits (furrows) on both E- and P-faces. (E) String gap junction, with step from E-face (E) to P-face (P), showing continuity of rows of E-face pits with P-face IMPs. The gap junction consists of ca. 16 connexons and is labeled for Cx32 by five 6 nm gold beads (*white arrowhead*) (LE=1:3). Unshadowed area has E-face pits (black arrow) faintly delineated by the carbon replica film. Unlabeled scale bars=0.1 μm.

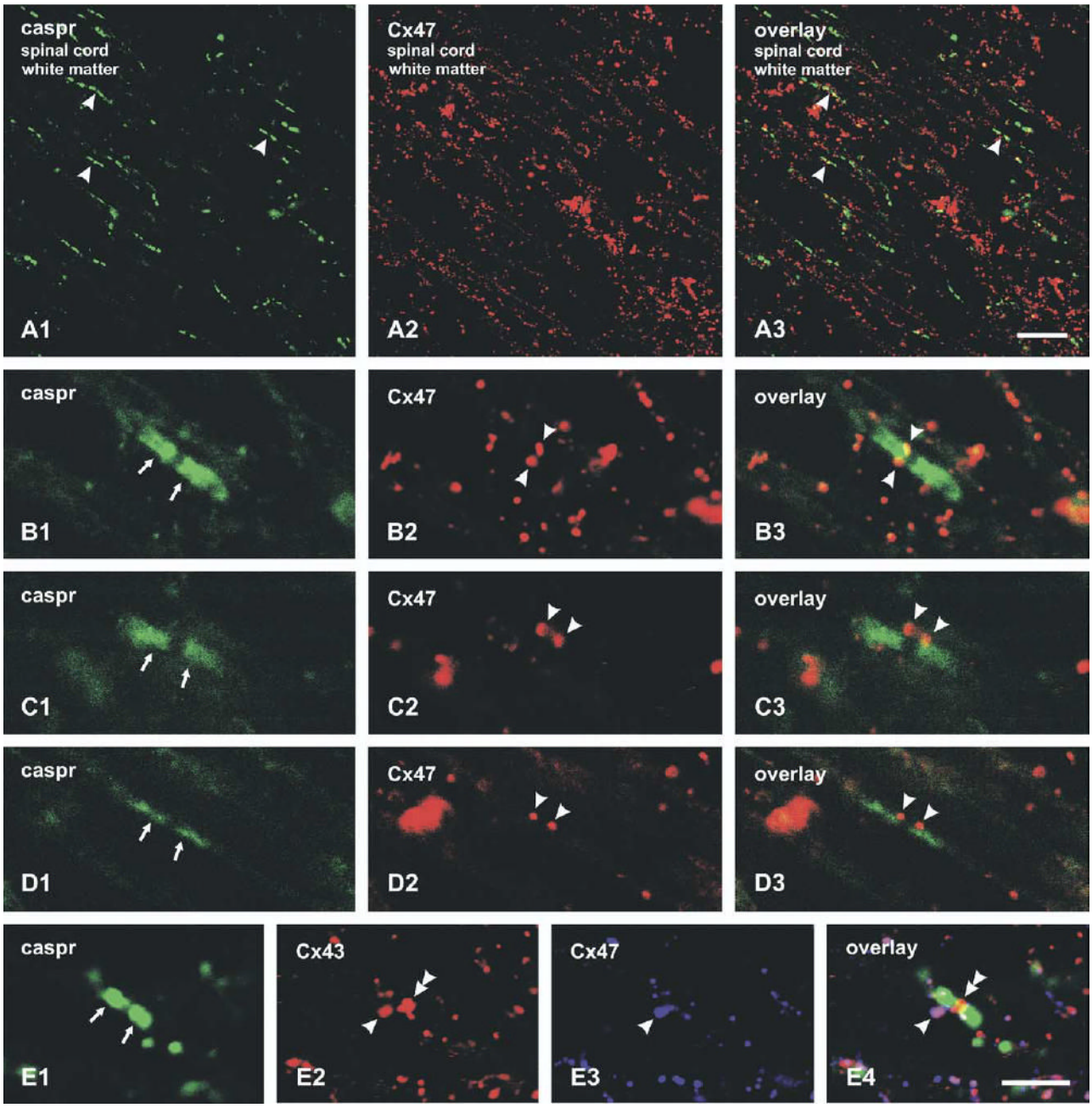

Fig. 9.

Laser scanning confocal double-immunofluorescence images of caspr and Cx47 labeling in white matter of adult rat spinal cord. (A) Low magnification of lateral white matter showing labeling of caspr at paranodal segments of nodes of Ranvier (A1, arrowheads) and linearly arranged labeling of Cx47 along myelinated fibers, with occasional co-association of immunolabeling (A3, arrowheads). (B–D) Higher magnifications of caspr-positive paranodes along large diameter fibers in lateral (B1, arrows) and ventral (C1, arrows) spinal cord white matter, and along a narrower fiber in lateral white matter (D1, arrows). In the same fields labeled for Cx47 (B2–D2, respectively), Cx47-positive puncta are seen closely apposed to the region of caspr-immunostaining immediately adjacent to the node of Ranvier (B3–D3, arrowheads). (E) Triple immunofluorescence showing labeling of caspr at a node of Ranvier

(E1, arrows), labeling of Cx43 adjacent to a caspr-positive segment (E2, arrowhead) as well as localized within the nodal area (E2 and E4, double arrowhead), and of Cx47 (E3, arrowhead), also adjacent to caspr and overlapping with Cx43 (E4, arrowhead). Scale bars=25 μm A; B–E, 5 μm.

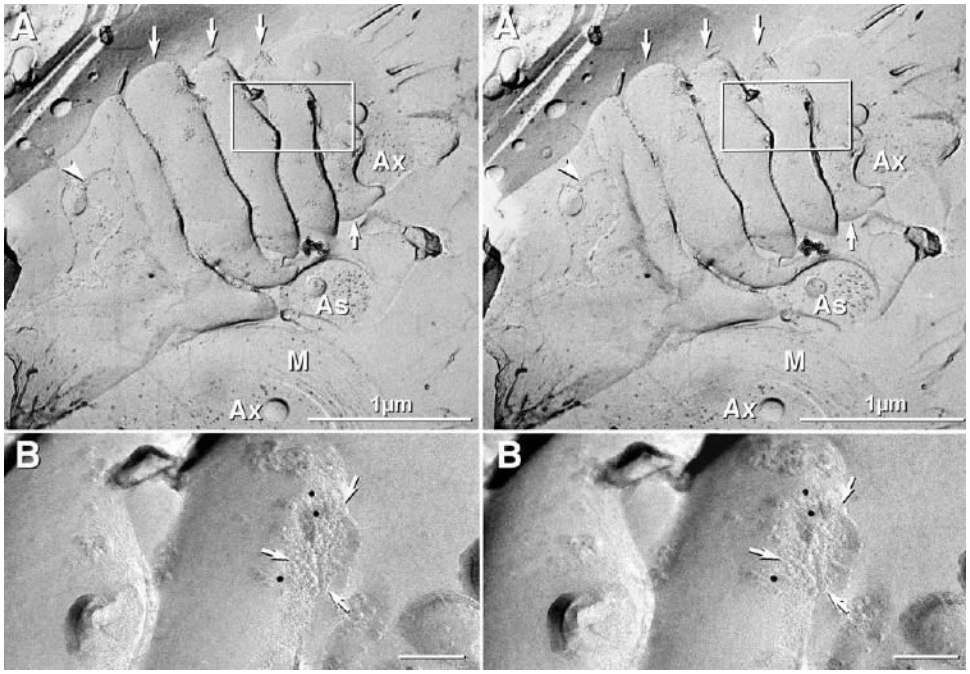

Fig. 10.

Stereoscopic FRIL images of gap junctions on everted loops of paranodal plasma membrane after immunogold labeling for Cx47. (A) Low magnification stereoscopic image revealing the outer surface of myelin (left side), including a small area where the fracture plane steps between three outermost layers of myelin (arrowhead). Four paranodal loops (arrows) extend beyond the outermost layer of myelin, there to contact astrocytes (As) in the nodal gap. The boxed area is shown at higher magnification and after tilting ca. 50°, thereby allowing en face viewing of an immunogold-labeled gap junction on the shoulder of a paranodal loop. (B) At higher magnification, the gap junction is seen to be immunogold labeled for Cx47 (three 12 nm gold beads). Arrows delineate the edge of the gap junction. Although insufficient area of the contacting cell is visible for positive identification, the image is consistent with coupling to one of the astrocyte processes that are common in this area (see Results for references). Ax, axon; M, cross-fractured myelin. Unlabeled scale bars=0.1 μm.

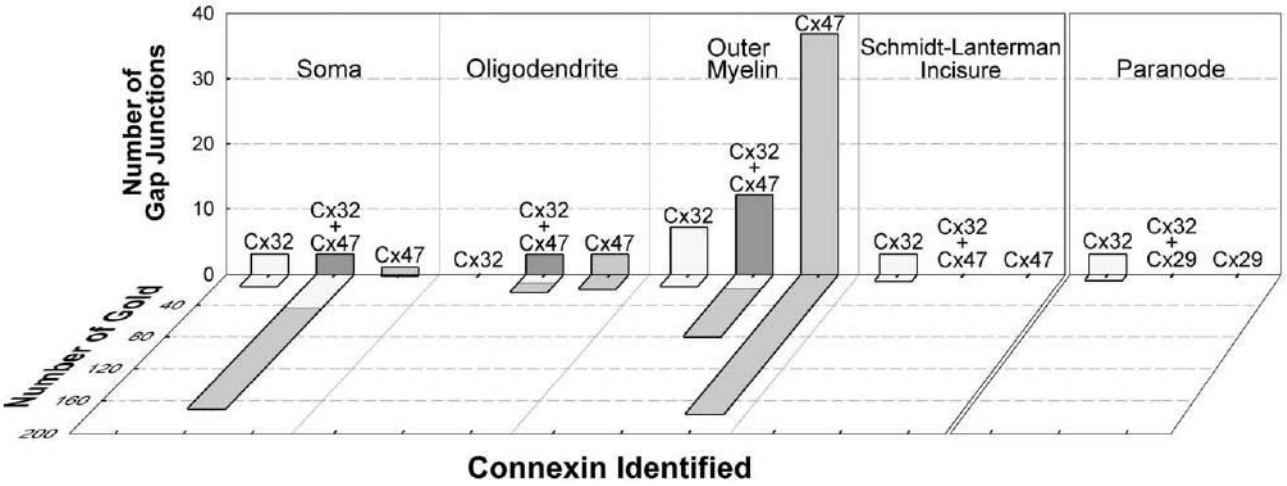

Fig. 11.

Histogram showing number of gap junctions and number of gold beads labeling Cx47 and Cx32 in each of the locations diagramed in Fig. 12A. The number of gap junctions was greatest on myelin (tallest gray bar), but the total number of gold beads was comparable on somatic vs. myelin plasma membranes (diagonal gray, white and gray-white bars). Cx47 was the predominant connexin on the outer surface of myelin (tallest gray bar). Cx32 (but not Cx47) was found in internodal gap junctions at Schmidt-Lanterman incisures, and Cx32 (but not Cx29) was found in paranodal gap junctions (right panel).

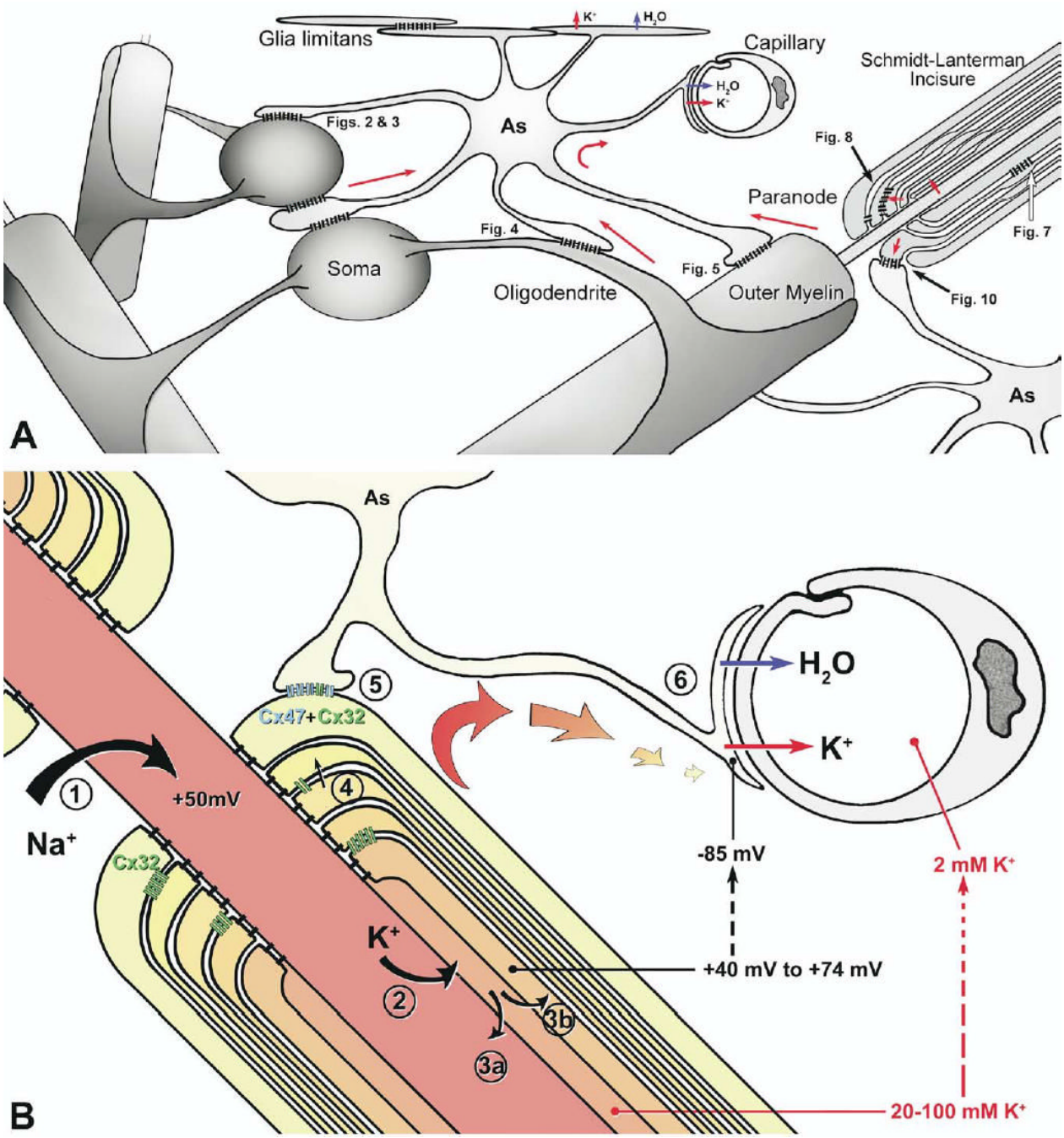

Fig. 12.

Diagram of locations of *heterologous* O/A gap junctions on oligodendrocyte cell body, dendrites, outer surface of myelin and everted paranodal loops, and *autologous* (i.e. interlamellar) gap junctions at Schmidt-Lanterman incisures and between paranodal loops (A), and pathways for "potassium siphoning" (B). (A) Astrocyte endfeet contacting capillaries and forming the glia limitans release excess K^+ ions (uppermost red arrows) and associated osmotic water (blue arrows) via Kir4.1 potassium channels (Hibino et al., 2004) and AQP4 water channels that are concentrated in the endfoot plasma membranes (Nielsen et al., 1997; Rash et al., 2004a). (B) Summary of movement of positive charge following an axon action potential. Red-to-yellow gradient=charge gradient from areas of excess positive charge/positive

membrane potential to lowest positive charge/highest negative membrane potential. Initial positive potential from entry of Na+ (arrow #1); excess positive charge in axon results in movement of K^+ into the inter-perinodal space (arrow #2). K^+ returns to the axon (arrow #3a) or enters the innermost cytoplasmic layer of myelin (arrow #3b), passes though successive paranodal loops (arrow #4), either circumferentially or through Cx32-containing gap junctions to the outermost cytoplasmic layer of myelin, then through Cx47/Cx32-containing gap junctions into the astrocyte syncytium (arrow #5), to astrocyte endfeet at capillaries and the glia limitans (arrow #6). Blue connexons, Cx47; green connexons, Cx32.

Table 1

Antibodies used for immunohistochemistry

Antibody	Type*	Epitope; designation	Reference; source
connexin29	Polyclonal	c-Terminus; 34-4200	(Li et al., 2002), Zymed
connexin32	Monoclonal	c-Terminus; 35-8900	(Nagy et al., 2003a,b), Zymed
connexin32	Polyclonal	Cytoplasmic loop; 71-0600	(Li et al., 1997), Zymed
connexin32	Polyclonal	c-Terminus; 34-5700	(Nagy et al., 2003a,b), Zymed
connexin32	Monoclonal	c-Terminus; Mab 3069	Chemicon
connexin43	Monoclonal	c-Terminus; 35-5000	(Nagy et al., 2003a,b), Zymed
connexin43	Polyclonal	c-Terminus; 71-0700	(Li et al., 1998), Zymed
connexin43	Polyclonal	aa 346–363; 18A	(Yamamoto et al., 1990a,b)
connexin43	Polyclonal	c-Terminus; sc-6560	Santa Cruz Biotech
connexin47	Polyclonal	c-Terminus; 36-4700	(Li et al., 2004), Zymed
connexin47	Monoclonal	c-Terminus; 37-4500	Zymed
caspr	Monoclonal	Extracellular; mab275	(Poliak et al., 2003)

*All monoclonal antibodies were from mouse and all polyclonal antibodies were from rabbit, except sc-6560 which was from goat. Anti-connexin antibodies were obtained from sources listed in Experimental Procedures, and as indicated above, with references to previous characterizations. The monoclonal antibody against the oligodendrocyte-specific paranodal marker caspr was generously provided by Dr. E. Peles (Weizmann Institute of Science, Rehovot, Israel).

Table 2

Number of labeled gap junctions observed at different subcellular locations in oligodendrocytes, and total number of immunogold beads associated with Cx32 and Cx47 at each subcellular location

	Cell location										
	Soma+dendrites			Outer myelin			Incisures			Paranodes	
Connexin	# GJ	# Gold Cx32	# Gold Cx47	# GJ	# Gold Cx32	# Gold Cx47	# GJ	# Gold Cx32	# Gold Cx47	# GJ	# Gold Cx32
Cx32 only	3	16	—	7	16	—	3	8	0	3	7
Cx32+Cx47	6	46	150	12	18	62	0	0	0	**	**
Cx47 only	4	—	20	37	—	180	0	0	0	*	*
Total junctions/ total gold	13	62	170	56	48	242	3	8	0	3	7
Total connexons	4410			4760			42			80	

* Labeled for Cx29; no Cx29 gold labels present at these locations.